

# Nickel in olivine as an exploration indicator for magmatic Ni-Cu sulfide deposits: a data review and re-evaluation

## REVISION 2

Stephen J. Barnes<sup>1</sup>, Zhuo-Sen Yao<sup>2</sup>, Ya-Jing Mao<sup>3</sup>, Ana P. Jesus<sup>4</sup>, Shenghong Yang<sup>5</sup>, Valentina Taranovic<sup>1,7</sup>, Wolfgang D. Maier<sup>6</sup>.

<sup>1</sup>CSIRO Mineral Resources, 26 Dick Perry Ave., Kensington, WA 6151 Australia.

Steve.barnes@csiro.au <sup>2</sup>Department of Earth Sciences, Carleton University, Ottawa, Canada.

yaozhuosen@gmail.com <sup>3</sup>Key Laboratory of Mineral Resources, Institute of Geology and Geophysics, Chinese Academy of Sciences (CAS), Beijing 100029, China. maoyajing@mail.iggcas.ac.cn.

<sup>4</sup>Faculdade de Ciências, Universidade de Lisboa, Lisbon, Portugal. [apjesus@fc.ul.pt](mailto:apjesus@fc.ul.pt) <sup>5</sup>Oulu Mining

School, Univ. of Oulu, Finland. shenghong.yang@oulu.fi. <sup>6</sup>Dept. of Earth Sciences, Univ. of Cardiff,

Wales. maierw@cardiff.ac.uk. <sup>7</sup>tinatskg@gmail.com.

### Abstract

Nickel contents of olivine have been widely used as petrogenetic indicators and as fertility indicators for magmatic sulfide potential of mafic-ultramafic intrusions, on the assumption that olivines crystallized from magmas that had equilibrated with sulfide liquid should be relatively depleted in Ni compared with a sulfide-free baseline. This has given rise to a large accumulation of data that is brought together here, along with data on volcanic olivines, to critically evaluate the effectiveness of the approach. We identify multiple sources of variance in Ni content of olivine at given Fo content, including: variability in mantle melt composition due to depth, water content (and possibly source); subsequent fractional crystallization with and without sulfide; recharge and magma mixing; batch equilibration between olivine and sulfide at variable silicate-sulfide ratio (R) and olivine/liquid ratio; and subsequent equilibration during trapped liquid crystallization in orthocumulates. Baselines for Ni in olivine in relation to Fo content are somewhat lower in orogenic belt settings relative to intrusions in continental Large Igneous Provinces (LIPs). This is probably related to differences in initial parent magma compositions, with plume magmas generally forming deeper and at higher temperatures. No clear, universal discrimination is evident in Ni in olivine between ore-bearing, weakly mineralized and barren intrusions even when tectonic setting is taken into account. However, sulfide-related signals can be identified at intrusion scale in many cases. Low-R factor, low-tenor sulfides are associated with low-Ni olivines in a number of examples and these cases stand out clearly.

31 Anomalously high-Ni olivines are a feature of some mineralized intrusions, in part due to trapped  
32 liquid reaction effects. However, in some cases, this mechanism cannot account for the magnitude  
33 of enrichment. In these cases, enrichment may be due to re-entrainment of “primitive” Ni-rich  
34 sulfide by a more evolved Fe-rich magma, driving the olivine to become Ni-enriched due to Fe-Ni  
35 exchange reaction between sulfide and olivine during transport. An extreme case of this process  
36 may account for ultra-Ni enriched olivine at Kevitsa (Finland), but more subtle signals elsewhere  
37 could be positive indicators. A lack of clear mineralized/barren distinction in specific groups of  
38 related intrusions, e.g. the deposits of NW China or the Kotalahti Belt in Finland, may well be due to  
39 “false negatives” where undiscovered mineralization exists in specific intrusions or in their feeder  
40 systems, or may also be due to a multiplicity of confounding factors. Wide variability of both Fo and  
41 Ni between related intrusions at regional scale may be a useful regional prospectivity indicator,  
42 more than an intrusion-scale discriminant, and is certainly informative as a petrogenetic indicator. In  
43 general, the use of Ni-olivine as a fertility tool is more likely to generate false negatives than false  
44 positives, but both are possible, and the technique should be used as part of a broader weight-of-  
45 evidence approach.

46 *Keywords: magmatic sulfides, nickel deposits, mantle melting.*

## 47 Introduction

48 The Ni content of olivine has been used over several decades as an indicator of potential host rocks  
49 to magmatic Ni-Cu sulfide deposits (Häkli, 1971; Naldrett et al., 1984; Li and Naldrett, 1999; Barnes  
50 et al., 2004; Makkonen et al., 2008; Barnes and Fiorentini, 2012; Le Vaillant et al., 2016). More  
51 generally, Ni in olivine has been widely used as a petrogenetic indicator to infer mantle magma  
52 sources (Sobolev et al., 2005; Sobolev et al., 2007; Li and Ripley, 2010) and deep-seated petrogenetic  
53 processes (Hart and Davis, 1978; Zhang et al., 2005; Herzberg et al., 2016; Matzen et al., 2017b;  
54 Gleeson and Gibson, 2019). Its potential usefulness as a prospectivity indicator arises from the  
55 compatible and chalcophile character of Ni, which has a strong tendency to partition both into  
56 olivine and much more strongly into sulfide liquid from coexisting silicate melt (Duke, 1979; Naldrett  
57 et al., 1984; Kiseeva and Wood, 2015; Yao et al., 2018). Consequently, competition for Ni between  
58 co-precipitating sulfide and olivine should produce olivine depleted in Ni relative to olivines that  
59 have never “seen” sulfide liquid. This effect was modelled in detail in the only previous global review  
60 of the topic (Li et al., 2007). However, more recent experimental data on the strong dependency of  
61 partitioning behaviour of Ni into olivine with temperature (Li and Ripley, 2010; Matzen et al., 2017a;  
62 Matzen et al., 2017b; Pu et al., 2021) together with effects of recharge and magma mixing (Gleeson  
63 and Gibson, 2019) introduce important confounding factors into the interpretation. Furthermore,

64 olivine compositions may be modified considerably by post-cumulus processes (Barnes, 1986) which  
65 can generate Ni enrichment in some circumstances (Barnes and Naldrett, 1985; Li and Naldrett,  
66 1999; Ding et al., 2010). These multiple factors, among others considered here, have not been fully  
67 considered in previous studies,

68 In this contribution, we combine an empirical data-driven approach with quantitative modelling of  
69 the various factors controlling olivine compositions in sulfide-saturated and undersaturated  
70 magmas. We employ a large compilation of data on Ni in olivine from volcanic and intrusive rocks,  
71 including all the published data we have been able to locate on mineralized and unmineralized  
72 mafic-ultramafic intrusive rocks over a wide range of ages and tectonic settings. From this dataset,  
73 we assess whether systematic differences exist that would enable reliable discrimination of  
74 mineralized intrusions. Such a tool would potentially be applicable in target selection at the early  
75 stage of regional exploration campaigns and also in vectoring towards mineralization in well-  
76 explored terranes. This approach has already been investigated for komatiite-hosted magmatic  
77 sulfide systems and shown to be effective at prospect scale in some cases, such as the Agnew-  
78 Wiluna Belt of the Yilgarn Craton (Barnes and Fiorentini, 2012; Le Vaillant et al., 2016), although  
79 signals are commonly confounded by flushing of mineralized lava channels post ore formation  
80 (Barnes et al., 2013b). Here we focus primarily on application to mineralization within small mafic-  
81 ultramafic intrusions in continental large igneous provinces (LIPs) and orogenic belts.

## 82 Method

83 Olivine chemistry data has been compiled from large number of literature sources listed in  
84 Supplemental Table 1 and from the GEOROC online database ([http://georoc.mpch-  
85 mainz.gwdg.de/georoc/](http://georoc.mpch-mainz.gwdg.de/georoc/))(Lehnert et al., 2000; Sarbas, 2008). Data plotting and data density  
86 contouring was done with the ioGas geochemical plotting software. In all cases data are from  
87 electron microprobe microanalysis, which typically reports Ni contents down to hundreds of ppm  
88 with precisions around 5-10% of measured abundance. Tabulation of individual precision estimates  
89 for the many dozens of different data sources was not attempted, but readers are referred to  
90 original sources (Supplementary Table 1) for further details. A full listing of data compilation used in  
91 this study is available at <https://zenodo.org/record/5787901> or via the CSIRO Data Access Portal at  
92 doi: (*to be advised*).

93 Samples were classified on the basis of volcanic/intrusive status (volcanic, small intrusions and large  
94 layered intrusions); combined tectonic setting and age (large igneous provinces and convergent  
95 margins, Phanerozoic and Proterozoic) and for intrusion samples, three categories of mineralization  
96 status of the host intrusion: M(ineralized), containing economic accumulations of Ni-Cu sulfide;

97 (D)isseminated, containing economic or sub-economic disseminated Ni-Cu sulfide mineralization  
98 only; and (B)arren, either no sulfide mineralization at all as far as is known, or only minor  
99 disseminations. These distinctions are inevitably somewhat arbitrary and based on best available  
100 data. In many of the plots, summary “data clouds” for particular groupings are represented as  
101 smoothed kernel data density contours determined in the loGas plotting software. In most cases  
102 except where stated contours enclose the 50<sup>th</sup> and 90<sup>th</sup> percentiles on data point density.  
103 Modelling calculations follow the procedures and assumptions of Yao et al. (2018). These are  
104 described in appendix 1.

## 105 Results

### 106 Background olivine compositions in Phanerozoic basalts

107 Compositions of olivine phenocrysts in basalts provide a useful baseline for comparison, in that they  
108 are least likely to have been modified by the processes that affect cumulate rocks in intrusions. A  
109 dataset of over 20,000 analyses, assembled by Sobolev and co-workers (Sobolev et al., 2007), is  
110 shown in summary form in Figure 1 along with additional data from convergent margin basalts from  
111 the GEOROC database (Sarbas, 2008). Wide variability was noted by Sobolev et al. (2007) in relation  
112 to tectonic setting, such as basalts from continental large igneous provinces (CLIPS) and from intra-  
113 oceanic plumes associated with old, thick oceanic lithosphere. This gives rise to distinctly different  
114 baseline ranges for CLIPS, oceanic LIPs and hotspot chains (OLIP) and MORBs, which are distinctly  
115 lower in olivine Ni than the other two categories for given Fo content. Since many of the potential  
116 target intrusions for magmatic sulfide deposits occur within mid-plate LIPs, the CLIP basalt dataset  
117 (Figure 1B) makes a useful baseline for comparison for these cases. The approximate 75<sup>th</sup> percentile  
118 data density contour on the CLIP data (black outline on Figure 1 B,C) (with the outlying  
119 Gudchichinsky Picrite suite from Siberia excluded) is reproduced in some of the diagrams that follow.

#### 120 *Figure 1*

121 Volcanic olivine compositions from convergent margins (Figure 1D) show a somewhat contrasting  
122 pattern with the LIP data cloud. The bulk of the data sets overlaps with the LIP data, but clusters of  
123 points fall both well above and well below. Oceanic arc olivines have a distinctly bimodal  
124 distribution, whereby a distinct group of primarily oceanic arc-associated olivines falls well below the  
125 LIP cloud at the higher Fo end (Fig. 1D).

### 126 Comparison of intrusion hosted olivines between tectonic settings

127 Modelling of olivine compositions from variably hydrated and variable depth sources (see below)  
128 indicates that we would expect significantly different baseline trends for magmas from deep-

129 sourced continental LIPs relative to magmas formed by shallow flux melting in arcs. The effect of  
130 melting depth (melting beneath thick and thin lithosphere) was pointed out by (Sobolev et al., 2005,  
131 2007). For this reason we combine continental LIP and intracratonic layered intrusions such as  
132 Bushveld together as one category, and orogenic belts with likely arc associations as another (Figure  
133 2) in establishing baselines for comparison of mineralized versus unmineralized intrusions. A caveat  
134 is needed here in that in some cases “orogenic belt” localities may be sampling plume magmas  
135 emplaced along craton margins and caught up in collisional events; this is particularly an issue in  
136 highly deformed Proterozoic orogens such as the Albany-Fraser Orogen in Western Australia. For  
137 purposes of this study, we include all such occurrence in the Orogenic Belt category but  
138 acknowledge the strong possibility of misclassification. Data for unmineralized intrusions only are  
139 plotted in Figure 2. Layered intrusions containing stratiform PGE Reef mineralization are considered  
140 unmineralized for this purpose, on the grounds that the magmas parental to the reefs could not  
141 have interacted previously with large proportions of sulfide liquid.

142 A major problem in empirical comparisons of this type is a sampling bias towards mineralized  
143 intrusions; they tend to be more common subjects of academic study than barren intrusions and  
144 exploration companies drill more holes into sulfide-bearing bodies. Furthermore, there may well be  
145 a false negative bias in that where an intrusion is known to contain sulfides its classification is clear,  
146 whereas “barren” intrusions may simply contain as yet undiscovered mineralization. As an  
147 additional baseline for comparison, we have therefore included a field for expected olivine  
148 compositions derived by fractional crystallization from the plausible range of mantle-derived basaltic  
149 magmas generated by 10% or more partial melting, based on the modelling of Yao et al. (2018). This  
150 field is labelled “MSFM” for “model sulfide free mantle melts” in Figure 2 and subsequent Ni vs Fo  
151 plots. The derivation of these model values is discussed in detail below.

152 *Figure 2.*

153 The data clouds shown in Figure 2 are clearly distinct between the continental LIP (CLIP+LMI) and  
154 Orogenic Belt (OB) categories, with the latter having consistently lower Ni for the same Fo content.  
155 We therefore need to consider different baselines for these two different tectonic settings.  
156 Furthermore, the data set for CLIP-associated intrusions shows a considerably broader spread than  
157 the field for volcanic olivines, particularly at low Fo contents.

158 In the following sections, we compare olivine compositions for mineralized and unmineralized  
159 intrusions from CLIP and OB settings. Implicit in this comparison is the major uncertainty of “false  
160 negatives” as noted above, which should be borne in mind through the discussion.

## 161 Mineralized vs barren, CLIP settings

162 Figure 3 shows a comparison of data points for olivines in variably mineralized mafic-ultramafic  
163 intrusions in intraplate continental Large Igneous Province (CLIP) settings (including large  
164 intracratonic layered intrusions), plotted over the data density cloud for unmineralized CLIP-  
165 associated intrusions. In this plot and those that follow, intrusions hosting economic sulfide-rich  
166 mineralization are plotted as red symbols, with symbol shapes indicating locality, while green  
167 symbols denote intrusions containing disseminated and/or minor subeconomic mineralization only.  
168 The bulk of the data fall within the “unmineralized” data cloud, with three localities as major  
169 exceptions. Kabanga (Tanzania) shows consistently strong Ni depletion in the main ore-hosting  
170 intrusion (Maier et al., 2010; Maier et al., 2011). Voisey’s Bay (Labrador, Canada, red circles) defines  
171 a field of widely varying Ni and Fo with Fe-rich olivine compositions extending to below Fo45. Nickel  
172 contents vary by a factor of up to 7 over the same Fo. In the Kevitsa Intrusion (northern Finland) the  
173 range of variability is a factor of 20 over a limited range in Fo. As well as a cluster of strongly  
174 depleted olivines, the Kevitsa dataset includes some extreme examples of Ni enrichment (Yang et al.,  
175 2013) falling outside the scale limits of this plot; these are discussed further below in the case-study  
176 section below. The main conclusion at this stage is that there is no universal evidence for consistent  
177 Ni depletion in mineralized compared with unmineralized intrusions, but distinct signals can be  
178 recognized in some specific cases. Wide variability for limited range in Fo appears to be the most  
179 consistent signal in mineralized intrusions. It is noteworthy that a large portion of the data cloud falls  
180 above the theoretical field (MSFM field on Figure 3) for olivines derived from sulfide-free mantle  
181 melts.

182 Figure 3.

## 183 Mineralized vs barren, orogenic belt settings

184 An exactly equivalent comparison to that in Figure 3 is shown in Figure 4 for combined Phanerozoic  
185 and Proterozoic orogenic settings (bearing in mind that some of the localities included in this  
186 category could be misallocated plume associations). The same conclusion applies: there is no clear  
187 evidence for consistent Ni depletion in mineralized compared with unmineralized intrusions.  
188 However, as in the CLIP category, mineralized intrusions occupy a wider range, with Ni falling both  
189 above and below the unmineralized baseline and show a wide variability of Ni for similar Fo  
190 contents. The most clearly anomalous mineralized intrusions are the Savannah intrusions in the Halls  
191 Creek orogen that show localized strong enrichment, and a group of intrusions (Moxie, Maine; St  
192 Stephen, New Brunswick and Rana, Northern Norway) within the Appalachian-Caledonide orogen  
193 that shows consistently Ni depleted olivine (Figure 4B). The Beja intrusion, Portugal, host to minor

194 disseminated sulfides (Jesus et al., 2020), straddles the 90th percentile “barren” contour but  
195 contains a high proportion of significantly Ni-depleted olivines at low Fo. We consider some of these  
196 localities further below as case studies. The Xiarihamu deposit in the East Kunlun orogenic belt in  
197 Tibet shows a distinctive signal of widely variable Ni at a restricted range of high Fo contents,  
198 somewhat similar to the Poyi intrusion in the Central Asia Orogenic Belt in China. Comparing  
199 Phanerozoic and Proterozoic settings, Phanerozoic intrusions appear to be more likely to show  
200 recognisable Ni depletion, as noted by Jesus et al. (2020). This may be an association with depth of  
201 emplacement, noting that several of the Proterozoic intrusions (Savannah, Kotalahti Belt, Nova)  
202 were emplaced at mid to lower crustal depths.

203 Compared with the theoretical model field for olivines derived from sulfide-free basalts (MSFM  
204 outline), evidence for Ni depletion is seen in the localities mentioned above, along with some  
205 samples from Xiarihamu, Ntaka Hill, Nova and several of the Chinese CAOB deposits. Samples from  
206 Savannah plot well above the MSFM field.

207 *Figure 4.*

## 208 **Comparison within individual magmatic provinces**

209 In this section, we consider some specific examples from both orogenic and CLIP categories where  
210 multiple intrusions co-exist within a restricted province with and without significant mineralization.

211 LIP related: Kabanga–Musongati–Kapalagulu Belt, Tanzania

212 The Kabanga deposit is located in a relatively small chonolith-style intrusion within the 1.4 Ga  
213 Kabanga–Musongati–Kapalagulu (KMK) mafic–ultramafic belt that extends for >500 km from Uganda  
214 to Lake Tanganyika in the Great Lakes region of East Africa (Deblond and Tack, 1999; Evans et al.,  
215 2000; Duchesne et al., 2004; Maier et al., 2007; Maier et al., 2010). This belt is considered to form  
216 part of a LIP developed along the NW margin of the Tanzanian Craton (Mäkitie et al., 2014). The belt  
217 contains both relatively large, mafic-ultramafic layered intrusions of several km thickness and tens of  
218 square km in surface and subsurface outcrop (e.g., Musongati and Kapalagulu) and numerous sills  
219 and chonolith bodies consisting largely of harzburgite, pyroxenite and gabbro, with  
220 thicknesses on the order of m to hundreds of m (e.g., Kabanga).

221 The Kabanga North-MNB body, one of the smallest intrusions in the belt, has a tubular chonolith  
222 morphology measuring up to 150 m in diameter. The body has been delineated by drilling for ~1.4  
223 km in a NE–SW direction. The Kabanga Main intrusion is a sill-like body with a relatively narrow  
224 (2km), trough-like lower portion and an upper segment of greater width (~4km). Its thickness may  
225 be on the order of 500m. The ~500-m-thick MNB body was discovered in 2001 while drilling for  
226 extensions of the Kabanga North body. The MNB extends over >2 km strike length and bears

227 considerable similarity to the Kabanga Main body. It may thus represent the extension of Kabanga  
228 Main at depth. The Block 1 intrusion, 4 to 5 km to the SW of Kabanga Main, consists of a thick (~  
229 800m) pile of mafic-ultramafic cumulates containing abundant disseminated low-tenor sulfides.  
230 The heavily mineralized intrusions of the Kabanga locality stand out clearly as having strongly Ni  
231 depleted olivines, with the most advanced depletion being in the Upper KM Sill, Block 1 and the  
232 MNB body (Figure 5). This is the clearest example in the entire dataset of strong Ni depletion  
233 associated with high degrees of crustal contamination and abundant sulfides having low Ni tenors.  
234 Kabanga sulfides have low Ni (<1–3 wt%), Cu (~0.1–0.4 wt%), and PGE contents (<<1 ppm), high  
235 Ni/Cu (5–15), and low Ni/Co (10–15) and Pd/Ir (2–20). Sulfides with higher metal contents (up to  
236 ~5% Ni, 0.8% Cu, 10 ppm PGE) are found in only one unit from Kabanga North, which significantly  
237 has markedly less Ni depleted olivine, albeit still depleted relative to the CLIP “Barren” baseline. The  
238 observed metal contents of the Kabanga sulfides are consistent with segregation of magmatic  
239 sulfides from fertile to strongly metal-depleted magmas, at intermediate to very low mass ratios of  
240 silicate to sulfide liquid (R factors) of approximately 10–400.

241 The Kapalugulu intrusion, approximately 300 km south of Kabanga, is a large layered intrusion  
242 containing chromitite and associated PGE concentrations. It contains sulfide mineralization only in a  
243 proposed feeder zone and shows undepleted olivines in samples from the unmineralized layered  
244 cumulate sequence.

245

246 *Figure 5.*

247 **Proterozoic Orogenic Belt: Halls Creek Orogen, Australia.** The Savannah (formerly Sally Malay) and  
248 Savannah North deposits, along with the smaller Copernicus deposit, are located within a belt of 1.8  
249 Ga mafic and mafic-ultramafic intrusions, the Sally Malay Suite, within the Halls Creek Orogen of  
250 Western Australia (Mole et al., 2018; Le Vaillant et al., 2020). The magmatism is thought to be  
251 related to a slab break-off event during the collision of the North Australian and Kimberley Craton  
252 (Kohanpour et al., 2017). The Savannah deposit occupies the lower edge of a now rotated bladed  
253 dyke (Barnes and Mungall, 2018) and the adjacent Savannah North deposit occupies a basal contact  
254 position within a separate small layered intrusion with probable funnel geometry. A group of  
255 petrographically similar intrusions within about 10 km of Savannah has been sampled by regional  
256 scale exploratory drilling, which has located only minor occurrences of disseminated sulfide. On this  
257 basis, Savannah and Savannah North samples represent the mineralized category while the  
258 remainder are considered barren.

259 Most of the olivines analysed from this suite fall within the “barren” baseline for orogenic settings  
260 (Figure 6), and Savannah North is indistinguishable in olivine chemistry from the barren Dave Hill and  
261 Wilson’s Creek bodies, aside from one data cluster at high Fo and low Ni that probably does reflect  
262 sulfide-related depletion. The notable exception is the Savannah Intrusion, which contains  
263 substantially more Ni enriched olivines within the layered peridotite and olivine norite layers that  
264 occupy the interior of the dyke. These rocks are primarily mesocumulates, and no systematic  
265 difference in olivine composition is recognisable with sulfide or olivine mode, such that the  
266 displacement from the cluster of Savannah North olivines cannot simply be explained by trapped  
267 liquid equilibration. The Savannah Intrusion evidently formed from a more Ni rich carrier magma  
268 than the other components of the Sally Malay suite. However, this contrast is not evident in the Ni  
269 tenors of the Savannah and Savannah North sulfide rich ores, which are 3.5-5 wt% and 2-3.5 wt%  
270 respectively. Both orebodies are strongly PGE depleted (Le Vaillant et al., 2020) implying prior  
271 extraction of sulfide liquid.

272 For this data set, we have also investigated the extent to which Fo-Ni variability is distinguishable on  
273 the basis of the sulfide content of individual samples (Figure 6B). Most of the analysed samples from  
274 the Savannah intrusion are sulfide-free, from the interior of the intrusion, showing the distinctive Ni  
275 enrichment characteristic of this body, but some mineralized samples are also Ni enriched. There is  
276 an almost complete overlap (with the exception of the highest Fo sample) between sulfide-bearing  
277 and sulfide-free samples in the Savannah North intrusion. This confirms that recognition of indicative  
278 Fo-Ni signals does not rely on sampling sulfide-bearing rocks.

279 *Figure 6.*

280 **Phanerozoic Orogenic Belt, Central Asian Orogenic Belt, NW China.** About a dozen economic  
281 magmatic Ni-Cu sulphide deposits occur at the southern margin of the Central Asian orogenic belt  
282 (CAOB) in NW China (Mao et al., 2008; Lu et al., 2019), with a few deposits occur in the  
283 southeasternmost part of CAOB, such as the Hongqiling deposit in NE China (Wei et al., 2013; Lu et  
284 al., 2019). These NW China deposits could be classified into four groups by spatial distribution: the  
285 Beishan, Central Tianshan, Eastern Tianshan, and south Chinese Altai groups from south to north.  
286 over a total distance of close to 1000 kilometres. They were predominately formed in the Permian  
287 (Qin et al., 2011; Su et al., 2011). The host rocks of these NW China deposits are enriched in hydrous  
288 phases and show arc-like geochemical characteristics, suggesting that the related magmas were  
289 derived from metasomatized mantle sources which have been modified by the subduction events  
290 prior to the Permian. Most researchers propose that the Permian magmatism in the south (Beishan,  
291 Central Tianshan, and Eastern Tianshan) of NW China was associated with the partial melting of  
292 metasomatized mantle driven by either the coeval Tarim mantle plume (Qin et al., 2011; Su et al.,

293 2011) or asthenosphere upwelling induced by lithosphere delamination (Song et al., 2011a; Zhang et  
294 al., 2011). The Permian magmatism in the Chinese Altai is thought to be triggered by a slab break-off  
295 event (Zhang et al., 2009; Li et al., 2012). Ore-hosting magmatic bodies of these deposits come in a  
296 variety of shapes, i.e. elongated rhomboid, kernel-shaped flares, tube-like or dyke-like, and have  
297 surface areas less than 2 km<sup>2</sup>. Several have been interpreted as variants on the theme of “blade-  
298 shaped dykes” (Barnes and Mungall, 2018). Sulphide mineralization mainly occurs at the bases of  
299 these magmatic bodies, with few exceptions locating at the central to upper zones, such as the  
300 Huangshandong mafic body and the Tulaergen deposit.

301 Olivine-rich cumulates are the predominant host to the sulphides in the NW China deposits.  
302 Lherzolite and olivine websterite are the most prevalent rock types in the intrusions, such as the  
303 Tianyu and Baishiquan deposits in the Central Tianshan, Huangshandong, Huangshanxi,  
304 Huangshannan, Xiangshanzhong, Tudun, Tulaergen, and Hulu deposits in the Eastern Tianshan.  
305 Dunite is one of the main rock types of the intrusions from the Beishan, such as the Poyi and Poshi  
306 intrusions (Xue et al., 2016). The Kalatongke deposit comprises 14 small mafic intrusions, with the  
307 orebodies mostly hosted by the Y1 and Y2 intrusion. Olivine grains are common in the Y1 intrusion,  
308 where olivine norite is the main rock type, but rarely found in the others. (Zhang et al., 2009; Gao  
309 and Zhou, 2013; Mao et al., 2021). The olivine from the NW China deposits has variable Fo values  
310 (from 70 to 90 mol%) (Figure 7). Generally, the Ni content in olivine decreases with decreasing Fo  
311 value (Figure 7), as expected for simple fractional crystallization. For each deposit, the Ni variation  
312 cannot be adequately produced by fractional crystallization alone. For instance, the Poyi olivines  
313 show wide Ni variation (from 1500 to 3500 ppm) but subtle Fo variation (88-89 mol%).

314 The intrusions of this province show no clear discrimination on the basis of olivine chemistry  
315 between mineralized and weakly or unmineralized intrusions (Figure 7). The mineralized  
316 Huangshanxi intrusion shows a wide range in Ni, 400-1750 ppm, over a restricted range in Fo, but  
317 similar ranges are seen in unmineralized and weakly mineralized bodies also. Huangshandong  
318 contains both Ni-depleted and Ni-enriched olivine at relatively low Fo contents, whereas Kalatongke  
319 shows a grouping of relatively Ni-enriched olivines at around Fo75 compared with the rest of the  
320 CAOB data set, although less enriched than the olivines at Savannah (Figure 6). Notably, these  
321 Kalatongke samples are primarily sulfide-bearing orthocumulates, whereas the more Fo-rich samples  
322 from Poyi and others are adcumulate to mesocumulates. Huangshannan stands out as having  
323 strongly Ni-enriched olivines relative to the rest of the province, and to orogenic-setting intrusions  
324 generally, over a range of Fo contents. The distinctive character of the Huangshannan and  
325 Kalatongke olivines may be related to trapped liquid effects, as discussed below. With reference to

326 the modelled sulfide-free olivine (MSFM) field, distinct depletion is seen in Tulaergen (most  
327 samples), Huangshanxi, Hunangshandong, Honqiling, Xiarihamu, and Poyi.

328 Also included in this comparison is the Xiarihamu deposit, a small ultramafic-dominated intrusion of  
329 Paleozoic age in the East Kunlun orogenic belt in Tibet, containing a large accumulation of  
330 disseminated sulfides (Li et al., 2015; Song et al., 2016; Song et al., 2020), entirely unrelated to the  
331 CAOB suite. It is marked by a very wide range of Ni contents at a relatively high and narrow range of  
332 Fo contents, similar to Poyi.

333 As in the previous section for the Savannah area intrusions, sufficient data are available to subdivide  
334 individual samples on their sulfide content (Figure 7B). Depletion signals are present in sulfide-free  
335 as well as sulfide-bearing samples from the same intrusion (e.g. Poyi, Honqiling), although Ni-  
336 enriched olivines (Kalatongke and Huangshandong) tend to be restricted to sulfide-bearing samples.  
337 This can be taken as evidence for Ni enrichment being due to trapped liquid equilibration effects,  
338 discussed further below.

339 *Figure 7.*

340 **Proterozoic orogenic belt: the Svecofennian (Raahe-Ladoga) Orogenic Belt, Finland.** The  
341 Svecofennian Orogenic Belt (also known as the Raahe-Ladoga Belt, or the Kotalahti Nickel Belt) is a  
342 Paleoproterozoic (1.88 Ga) belt of polydeformed gneisses and amphibolites extending through  
343 central Finland (Makkonen et al., 2008; Makkonen, 2015). It is co-eval and probably correlative with  
344 the Vammala Nickel Belt in the south west of Finland. The belt contains over a dozen distinct mafic  
345 and mafic-ultramafic intrusions, several of which – Rytiky, Kotalahti, Hitura and Enankoski – contain  
346 mined or subeconomic Ni-Cu sulfide deposits (Makkonen et al., 2008; Makkonen, 2015), along with a  
347 suite of mafic metavolcanic rocks at least some of which are considered to be co-magmatic with  
348 these intrusions (Barnes et al., 2009). Most of these intrusions are deformed and in some cases  
349 dismembered and are considered to have been emplaced during the peak of metamorphism in the  
350 belt (Makkonen et al., 2015). The weakly differentiated, dominantly ultramafic Vammala-type  
351 intrusions consist almost entirely of olivine cumulates and represent magma conduits. The more  
352 strongly differentiated, mafic and mafic-ultramafic, Kotalahti type intrusions consist of olivine  
353 cumulates, pyroxene cumulates, and plagioclase-bearing cumulates. The parental magma was  
354 basaltic with MgO contents mostly around 10–12 wt%. The mineralized intrusions show chemical  
355 evidence for crustal contamination. Makkonen et al. (2008) identified Ni-depleted olivine in the  
356 mineralized intrusions. Some of the mineralized intrusions contain complexly zoned cumulus and  
357 poikilitic pyroxenes, features not observed in similar rock types from the unmineralized bodies  
358 (Schoneveld et al., 2020).

359 A new compilation of olivine data drawing on Makkonen et al. (2008) and Lamberg (2005) is shown  
360 in Figure 8. There is no clear-cut discrimination between the mineralized and barren intrusions, but  
361 some indicative features are present. Distinct depletion is evident at low Fo contents in the weakly  
362 mineralized Ylivieska intrusion; the mineralized Rytky intrusion shows a wide range in Ni from 600 to  
363 2400 ppm for a restricted range of 81-84 mol % Fo; the Nirimaki intrusion shows a similar trend to  
364 Rytky but displaced to lower Fo; and the weakly mineralized Laukukangas body shows a grouping of  
365 high-Ni, low Fo olivine similar to those seen at Kalatongke in the CAO (Figure 7). Data for several of  
366 the intrusions (Luusniemi, Ylivieska, Heimovouri) fall to the lower Ni end of the range of Ni in this  
367 tectonic setting, and well below the data cloud for plume-related settings.

368 *Figure 8.*

369 **Ural-Alaskan Complexes.** Ural-Alaskan Complexes are a rare but widely distributed component of  
370 orogenic belts in the Phanerozoic and Proterozoic, and in some cases contain sub-economic Ni-Cu  
371 sulfide mineralization, usually in the form of disseminated sulfides (Thakurta et al., 2008). Examples  
372 of this are the Duke Island Intrusion in Alaska (Li et al., 2013; Thakurta et al., 2014) and the  
373 Turnagain Complex in British Columbia (Clark, 1980). Olivine data from these intrusions are  
374 compared with the data contours on barren orogenic belt intrusions in Figure 9. Duke Island and  
375 some samples from Turnagain, along with the Akarem Complex in Egypt, which also contains  
376 disseminated mineralization (Helmy and Mogessie, 2001) contain distinctly Ni-depleted olivines  
377 falling well below the reference field and showing wide variability in Ni for limited Fo.

378 *Figure 9.*

379 **The Kevitsa intrusion, Finland.** The 2.058 Ga Kevitsa intrusion (Mutanen, 1997; Santaguida et al.,  
380 2015; Luolavirta et al., 2017; Luolavirta et al., 2018) is located in the Central Lapland greenstone belt  
381 in northern Finland. It is part of a suite of small to medium sized mafic-ultramafic intrusions,  
382 including the large Koitelainen layered intrusion as well as the neighbouring Sakatti intrusion hosting  
383 the Cu-Ni Sakatti deposit. These intrusions range in age from 2.1 Ga to 1.8 Ga (Huhma et al., 2013).  
384 They are emplaced into a volcanic suite containing komatiites. The Kevitsa intrusion occupies a  
385 surface area of approximately 16 km<sup>2</sup> and consists of a lower ultramafic unit up to 2 km in thickness,  
386 overlain by a mafic unit over several hundred metres thick. The ultramafic unit is composed of  
387 interlayered olivine pyroxenite and websterite, with local development of cyclic units, but for the  
388 most part lacking obvious internal layering (Santaguida et al., 2015), but showing inward-dipping  
389 cryptic layering defined by variations in the sulfide tenors (Le Vaillant et al., 2017). The Kevitsa Ni-Cu-  
390 (PGE) deposit occurs in the middle part of the ultramafic unit, associated with variably layered  
391 olivine pyroxenites and websterites. The deposit consists entirely of disseminated sulfides with  
392 widely varying Ni, Cu and PGE tenors, with a published combined resource of 237 Mt at 0.28% Ni,

393 0.41% Cu and 0.6 ppm 3E (Pt + Pd + Au) (Geological Survey of Finland website, 2016) with Ni grades  
394 up to around 0.6% (99th percentile on all assays in the database). The mineralization has been  
395 separated into different ore types, mainly on the basis of their Ni-PGE tenors showing a broadly  
396 layered distribution with higher tenors generally at higher levels within the stratigraphy (Le Vaillant  
397 et al., 2017). Low tenor disseminated but locally net-textured ores form near the base of the  
398 intrusion and along the margins of the Cu-Ni mineralization are classified as “false ore”. This  
399 pyrrhotite-rich mineralization has Ni tenors less than 1% and is typically associated with abundant  
400 country rock xenoliths. The “regular” or “normal” ore represents the bulk (>90%) of the economic  
401 resource and is characterized by 2–6 vol% of sulfides (pyrrhotite, pentlandite, and chalcopyrite) and  
402 average Ni and Cu ore-grades of 0.3 and 0.4 wt% respectively (Santaguida et al., 2015) with a range  
403 of Ni tenors between 1 and 10 % and PGE tenors between about 1 and 5 ppm. The volumetrically  
404 minor “Ni–PGE ore” has a similar sulfide content to that of the Normal ore, but the sulfides are  
405 predominantly pentlandite, pyrite and millerite. These ores have higher and more variable Ni grades,  
406 lower Cu grades (Ni/Cu = 1.5–15), and extreme Ni tenors ranging as high as 30%, attributed to high R  
407 factors in olivine-rich suspensions (Barnes et al., 2013a) with a likely, possibly assimilated komatiitic  
408 component (Yang et al., 2013). Pockets of Ni-PGE ore are developed throughout the orebody but the  
409 main development is in the upper part of the section (Le Vaillant et al., 2017).

410 The Kevitsa occurrence provides a useful case study in the variability of olivine compositions (Figure  
411 10) within a single extensively mineralized intrusion that shows a wide range in nickel tenors. The  
412 most striking feature of the dataset is the presence of a group of ultra-Ni-rich olivines within the Ni-  
413 PGE ores (Yang et al., 2013), but the dataset is also characterized by strongly Ni-depleted olivines  
414 associated with the very low Ni-tenor False Ores (Luolavirta et al., 2017). The False Ores are  
415 interpreted to be the opposite case to the Ni-PGE rich ores: the result of very restricted equilibration  
416 between abundant assimilated sulfide and a poorly-stirred, high viscosity crystal mush (Le Vaillant et  
417 al., 2017), or alternatively as the result of extensive pre-emplacement fractional extraction of sulfide  
418 (Luolavirta et al., 2018). Within the strongly Ni-enriched part of the data set, distinct linear arrays are  
419 developed at sample scale where Ni correlates negatively with Fo (Figure 10B): this is a hallmark of  
420 sample-scale trapped liquid equilibration, as discussed further below.

421 *Figure 10.*

422 **Nova-Bollinger.** The Mesoproterozoic Nova – Bollinger Ni-Cu – sulfide ore deposit is located in the  
423 Albany-Fraser Orogen in Western Australia (Maier et al., 2016). The host-rocks are mafic - ultramafic  
424 intrusive cumulates subdivided into two connected intrusions, designated Upper and Lower (Figure  
425 11). The Upper Intrusion is bowl-shaped and modally layered with alternating peridotite and norite  
426 mesocumulate layers, with a basal series of dominantly orthocumulate mafic lithologies. The Lower

427 is a much thinner semi-conformable chonolith (flattened tube-shaped intrusion) comprising mostly  
428 unlayered mafic to ultramafic orthocumulates (Taranovic et al., 2021). The Lower Intrusion hosts all  
429 the high-grade mineralization and most of the disseminated ores. A distinctive plagioclase-bearing  
430 lherzolite containing both orthopyroxene and olivine as cumulus phases is a characteristic of the  
431 Lower Intrusion and the basal series of the Upper. The intrusions were emplaced under peak  
432 metamorphic conditions at around 20-25 km depth into granulite facies paragneisses which  
433 underwent partial melting during extensive infiltration of sulfides into the footwall (Barnes et al.,  
434 2020). The geometry of the intrusions and the disposition of the sulfides suggest that the Lower  
435 intrusion formed as an apophysis off the base of the Upper, propagating westward into the footwall  
436 rocks (Taranovic et al., 2021). Nova-Bollinger ores contain Ni tenors in the 5-9% range (Barnes et al.,  
437 2021).

438 *Figure 11.*

439 A wide spread of Ni and Fo contents is present. The most Ni-depleted Fo rich olivines are located  
440 within the upper part of the Upper Intrusion, and also within the Lower intrusion where the two  
441 intrusions diverge. Less Fo rich olivines with trends towards Ni enrichment are in the Lower (ore-  
442 bearing) intrusion (Figure 11). The Lower Intrusion rocks are distinctly more orthocumulate such that  
443 the trend towards lower Fo and higher Ni can be attributed to trapped liquid effects, as discussed  
444 further below. This is particularly clear in the purple diamond symbols in Figure 11A. However, the  
445 most significant feature of the Nova data set is the presence of a widespread group of low-Ni, high-  
446 Fo samples located predominantly in the Upper Intrusion, and particularly in the entirely  
447 unmineralized layered ultramafic cumulates higher in the sequence (Figure 11B). This is significant  
448 from an exploration viewpoint in that the Lower Intrusion is entirely blind to the surface; recognition  
449 of Ni depletion in these ostensibly barren upper cumulate layers would be a pathfinder to the  
450 orebodies.

451 The choice of baseline for Nova is problematic. While the setting is undoubtedly a convergent  
452 margin orogenic belt (Spaggiari et al., 2015), the Fraser Zone magmatic complex to which Nova  
453 belongs is a large volume mafic suite with a restricted age range and trace element characteristics  
454 that could be interpreted as plume-like, indicative of a LIP affinity (Taranovic et al., 2021). If the  
455 Fraser Zone is indeed a LIP, then the low-Ni, high Fo olivines of the Upper intrusion are definitively  
456 depleted. Regardless, the Ni in olivine signal of the Nova-Bollinger intrusions is clearly positive for  
457 mineralization.

## 458 Discussion: controls on olivine Fo-Ni variations in sulfide-bearing 459 magmatic systems

460 As we have seen, intrusion-hosted olivines show wide and complex variability in Ni-Fo trends, even  
461 within the same intrusion, indicating that sulfide melt equilibration is only one of a number of  
462 factors influencing the Ni content of olivine. Some of these factors are considered and modelled in  
463 the following section.

### 464 Range of variability of Ni in carrier magmas

465 The silicate magmas that form magmatic sulfide ores (carrier magmas) are known to have a wide  
466 range of Ni contents, from ~1600 ppm in primitive komatiites to ~100 ppm in some mafic-hosted  
467 systems (Barnes et al., 2016). The ability of relatively low-Ni mafic magmas to form deposits with  
468 economic Ni contents arises from the very high partition coefficient  $D_{Ni}$  of Ni between sulfide and  
469 olivine; this  $D_{Ni}$  value increases strongly with falling temperature and hence is considerably higher in  
470 basalt than in komatiite (Kiseeva and Wood, 2015). The same effect applies to  $D_{Ni}$  between olivine  
471 and silicate melt (Li and Ripley, 2010; Matzen et al., 2013; Matzen et al., 2017a; Matzen et al.,  
472 2017b; Pu et al., 2021). The effect of this T dependence on olivine Ni contents gives rise to the  
473 observed wide variability in the Ni contents of primary mantle melts, (Li and Ripley, 2010; Yao et al.,  
474 2018) and basalt-hosted olivines (Sobolev et al., 2007; Herzberg et al., 2016), (Figure 1), a variability  
475 that could be further enhanced by variability in the pyroxene:olivine ratio in mantle sources (Sobolev  
476 et al., 2005). The presence of pyroxene-rich mantle-source regions has been proposed as a major  
477 controlling factor on the range of olivine compositions in various Chinese deposits (Song et al.,  
478 2011b; Song et al., 2011c; Lu et al., 2019), but remains a hotly debated topic beyond the scope of  
479 this contribution.

480 We have carried out a series of model calculations on compositions of potential carrier magmas and  
481 associated olivines generated at a variety of depths and primary water contents and undergoing  
482 fractional crystallization, following the methods of Yao et al. (2018). A representative series of these  
483 curves are shown in Figure 12, for conditions corresponding to sulfide undersaturation (i.e. no  
484 sulfide liquid involved during melting or fractional crystallization) and appropriate values for the  
485 crystallization pressure (1 kbar), water content (1 wt% H<sub>2</sub>O) and oxygen fugacity (QFM-1). The  
486 emplacement depths of most these mafic-ultramafic intrusions are probably shallow, resulting in a  
487 relatively narrow pressure range varying from 0.5 to 2.5 kbar (Norilsk, (Yao and Mungall, 2021);  
488 Bushveld, (Maier et al., 2013)), which has little influence on the trendlines of Ni in the crystallized  
489 olivine grains (Appendix Fig. A1-a). The addition of water into the parental magma will decrease the  
490 olivine saturation temperature and enhance the olivine stability during crystallization (dropping to a

491 lower Fo number), but the partition coefficient of Ni between olivine and melt has been shown to  
492 have a negligible dependence on water content (Pu et al., 2021). The combined effects of water  
493 content on the Ni trendlines of olivine grains is confirmed to be slight when the initial H<sub>2</sub>O in the  
494 parent magma varies from 0 to 3 wt% (Appendix Fig. A1B). The oxygen fugacity of plume-associated  
495 magmatism may mostly vary from QFM-2 to QFM, while the parental magma derived by flux-melting  
496 of mantle wedge can have a higher oxygen fugacity that can even reach QFM+2. These most oxidized  
497 conditions are within the range where most of the S in the magma would be dissolved as S<sup>6+</sup> rather  
498 than S<sup>2-</sup> such that sulfide formation is inhibited (Jugo et al., 2005), so can be disregarded in this  
499 context. In both settings, for  $fO_2$  below QFM+1, the variation of  $fO_2$  simply drives a limited horizontal  
500 movement of the trendlines of Ni contents (Appendix Fig. A1C, D) because a higher  $fO_2$  results in the  
501 increase of Fe<sup>3+</sup>/Fe<sup>2+</sup> in melt, which further elevates the Fo content of olivine. Hence, the variations  
502 of crystallization conditions have only a limited impact on the modelled Ni trendlines. The reader is  
503 referred to Appendix 1 for more detailed discussion of the modelling.

504 These curves are used to define a range for model olivine compositions that can be derived from  
505 plausible mantle partial melts, taking the upper limit as the uppermost plume model curve at any Fo  
506 and the lower as the 10% partial melt in the depleted MORB mantle (DMM) flux model. This range is  
507 plotted as a reference field on the data plots shown above.

508 Aside from this reference field, the main conclusions from the modelling are

- 509 1. the curve for olivine fractionation in plume magmas changes over a factor of about 50%  
510 (2400 to 3600 ppm) between pyroxenite-free and 30% pyroxenite sources, but converges to  
511 similar values with fractionation. The range between sources gives model trends that match  
512 reasonably well with the CLIP basalt data array, but fall to the low end compared with  
513 intrusion-hosted olivines.
- 514 2. Models involving flux melting from hydrated depleted mantle generate lower Ni in olivine  
515 for the same Fo, but also (probably for the same reason) fall at the lower Ni side of the field  
516 for intrusion hosted olivines. Natural olivines from convergent margin lavas show a wide  
517 spread of Ni at high Fo contents.

518 *Figure 12*

519 The consistent difference between olivine Ni contents in LIP relative to orogenic belt settings above  
520 probably arises largely from these primary controls on the compositions of the carrier magmas.  
521 More generally, it provides a major confounding effect on the ability to discern sulfide extraction  
522 history in magma suites from olivine compositions alone, reinforcing the need to use different  
523 baselines when comparing LIP settings with convergent margin settings.

## 524 Fractional crystallization of olivine + sulfide liquid

525 In most models of olivine evolution in sulfide-saturated systems, sulfide is assumed to be segregated  
526 from the carried magma along with the fractional crystallization of olivine in some defined  
527 proportion. In the models shown in Figure 13, olivine compositions are shown for fractional  
528 crystallization of two starting liquids: a plume melt including a 50% contribution from a “pyroxenite”  
529 mantle corresponding to the uppermost curve in Figure 12A, and from a melt generated by flux  
530 melting of depleted mantle (Figure 12B) as the proportion ratios of olivine and sulfide in each  
531 crystallization increment are assumed as 50, 100, 200 and 500. The partition coefficient of Ni  
532 between sulfide and melt is from the formulation of Kiseeva and Wood (2015). As expected,  
533 variation in the proportion of olivine to sulfide from 50 to 500 produces a change over a factor of 4-5  
534 in Ni in olivine. Various estimates of the proportion of sulfide to olivine under cotectic conditions  
535 (i.e. fractionation of olivine plus sulfide liquid exactly along the sulfide saturation surface) have been  
536 made, using various parameterizations of the sulfide content at sulfide liquid saturation (SCSS) as a  
537 function of melt chemistry and temperature (Ariskin and Barmina, 1999; Li and Ripley, 2005; Barnes,  
538 2007; Ariskin et al., 2013; Godel et al., 2013) with a general consensus of values around 100-200 for  
539 olivine saturated magmas. Hence cotectic fractionation should result in Ni depletion by factors of  
540 around 3-4.

541 *Figure 13*

## 542 Recharge and magma mixing

543 Recharge and magma mixing of derivative fractionated magmas with primitive parental magmas has  
544 been identified in MORBs and other mafic suites and has been proposed by Gleeson and Gibson  
545 (2019) as a mechanism for generating anomalous Ni enrichment in olivine. This follows from the  
546 convex-upward form of curves for Ni vs Fo in olivine during fractional crystallization (Figure 12,  
547 Figure 13). This type of process may account for otherwise unexplained Ni-enriched olivine trends  
548 such as in the Gudchichinsky Picrites of the Siberian LIP (Figure 1A), and also the high Ni in Hawaiian  
549 picrite olivines reported by Sobolev et al. (2007). Where magmatic sulfides are generated within  
550 multiply recharged sill-dyke networks, as proposed by Barnes et al. (2016), this process has good  
551 potential to obscure Ni depletion signals and indeed to generate enrichment. Presence of sulfide in  
552 the system may enhance this tendency, as discussed further below.

553 Gleeson and Gibson (2019) point out that recharge and mixing provides a viable alternative  
554 hypothesis to the “pyroxenite source” model, which has been involved for some Ni deposits and  
555 camps, notably several of the Chinese deposits (Lu et al., 2019). Numerous other studies (Matzen et  
556 al., 2017b; Yao et al., 2018) have pointed out other combinations of melting depth and mechanism

557 that avoid the need for pyroxenitic sources. Full discussion of this issue requires consideration of  
558 trace elements and isotopic signals that are out of scope of this contribution, but we note that of the  
559 deposits represented in this compilation, only a few (Mirabela, Poyi, Xiarihamu, Eagle and Kevitsa)  
560 contain olivines in the high Fo (>85 mol pct) and high Ni (>3000) ppm that are claimed by Sobolev et  
561 al (2007) as evidence for pyroxenitic mantle sources.

## 562 R factor effects

563 The term “R-factor” refers to the widely used equation (Campbell and Naldrett, 1979) describing the  
564 composition of silicate and sulfide melt during closed-system batch equilibration, where R is defined  
565 as the mass ratio of silicate to silicate liquid at equilibrium during a closed-system batch  
566 equilibration event. The equation can readily be adapted to also include olivine as a third component  
567 in the reaction (Barnes et al., 2013a). It is particularly applicable to the situation where a sulfide  
568 xenomelt (Leshner, 2017) is incorporated into a magma body by assimilation of crustal rocks and  
569 equilibrates with a fixed mass of magma. Olivine and sulfide compositions can be modelled by a one-  
570 stage three-way batch equilibrium calculation, involving equilibrium between olivine, sulfide liquid  
571 and silicate liquid using experimental values for partition and distribution coefficients (Barnes et al.,  
572 2013a). Figure 14 shows the results of these calculations for variable R and four hypothetical silicate  
573 melt compositions (Table 1): komatiite (“kom”), a high-Mg plume basalt (“Plume bas 18”), a  
574 ferropicrite and a MORB, using typical values taken from data compilations of Barnes and Fiorentini  
575 (2012) and Barnes et al. (2015). The main conclusion from the model results in Figure 14 is that  
576 much of the spread of Fo and Ni concentrations in olivine found between individual deposits can  
577 theoretically be explained by the combination of initial melt composition and R factor. Variations in  
578 R within a single deposit, as for example in the Kevitsa intrusion noted above, can generate the  
579 observed spread in olivine Ni for a limited range of Fo, and this variability would be expected to  
580 correlate with sulfide tenor, as indeed it does at Kevitsa. The prime cause of strongly Ni depleted  
581 olivine is equilibration with silicate and sulfide liquid at low R values, a process which generates  
582 correspondingly low-Ni tenor sulfides, as seen in the Kabanga example above (Figure 5) and  
583 modelled in Figure 14.

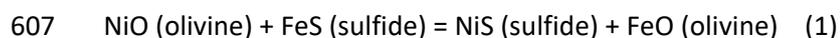
584 It is commonly concluded that depletion of Ni in olivine necessarily implies that the silicate  
585 component has been depleted by some previous “upstream” sulfide extraction event prior to the  
586 crystallization of the assemblage being studied; i.e. that the depletion implies the existence of an  
587 additional sulfide body or bodies elsewhere in the intrusion network. Figure 14 shows that this is not  
588 a necessary conclusion: a single stage batch equilibration event can produce a wide range in degrees  
589 of Ni depletion depending on the R factor. Low R factor, low Ni-tenor sulfide necessarily coexists  
590 with low-Ni olivine at equilibrium.

591 *Figure 14.*

592 *Table 1.*

### 593 **Trapped liquid effects**

594 One of the factors affecting cumulus mineral compositions is the effect of equilibration between  
595 olivine and trapped intercumulus liquid (Barnes, 1986). The principle is illustrated in Figure 15. The  
596 original orthocumulate consists of a mixture of olivine, sulfide and silicate liquid, assumed to be in  
597 equilibrium (Figure 15A), with the composition of the three phases determined by the three-way  
598 equilibration at a given R factor (mass ratio of silicate to sulfide) and proportion of silicate to olivine  
599 (F). In the illustrative calculations shown here, the proportion of olivine participating in this initial  
600 bulk equilibrium is assumed to be small, 5%. Olivine and sulfide then accumulated mechanically in  
601 different proportions along with a component of trapped interstitial silicate melt to form a partially  
602 solid mush (Figure 15B). For simplicity we assume that the resulting component has 40% trapped  
603 liquid and 5% sulfide (at and above this proportion of sulfide, the change in composition of sulfide  
604 during the trapped liquid reaction is minor). As the olivine then re-equilibrates with the evolving  
605 trapped liquid during solidification (Figure 15C), it becomes more Fe-rich, and consequently is  
606 constrained to also become more Ni rich due to the exchange reaction



608 The distribution coefficient for this reaction  $K_D$  is given by

$$609 K_D = (X_{\text{NiS}}/X_{\text{FeS}})_{\text{sulfide liquid}} / (X_{\text{NiO}}/X_{\text{FeO}})_{\text{olivine}}, \quad (2)$$

610

611 which has a value independent of temperature but dependent on  $fO_2$  and the sulfide  
612 composition (Brenan 2003; Barnes et al., 2013a; Mao et al., 2017).

613 The sulfide is the dominant reservoir of Ni in the rock for abundances of more than about 5%, such  
614 that its composition is only slightly affected by the trapped liquid reaction. Consequently, as the FeO  
615 content of the olivine increases, the NiO content must also increase to satisfy the  $K_D$ . This gives rise  
616 to a negative correlation between Fo and Ni, first recognized in the JM Reef of the Stillwater  
617 Complex (Barnes and Naldrett, 1985) and identified subsequently at Voisey's Bay (Li and Naldrett,  
618 1999). Hints of such correlations are present in several of the data sets presented in this study,  
619 notably Kevitsa (Figure 10).

620 *Figure 15.*

621 The effect has been quantified for a variety of different starting compositions and assumptions  
622 (Figure 16), using an iterative solution method based on that of Barnes et al. (2013a). The calculation

623 procedure involves (1) calculation of olivine, sulfide and liquid compositions for each starting liquid  
624 (Table 1) as a function of silicate:sulfide mass ratio  $R$ , corresponding to stage A in Figure 15; and (2)  
625 calculation of new olivine and sulfide composition following complete equilibrium crystallization of a  
626 mixture of 55% olivine, 5% sulfide and 40% trapped silicate liquid (Figure 15 b-c).

627 *Figure 16.*

628 The calculation shows that trapped liquid reaction can have a significant effect on Ni content of  
629 olivine, most evident in sulfide-bearing orthocumulates where the change in olivine Fo content is  
630 greatest. For komatiites, the effect is enhanced by the composition dependence of the  $K_D$  on the Ni  
631 content of the sulfide, which becomes a significant factor where the Ni content of the sulfide is in  
632 the 20-30% Ni range (Barnes et al., 2013a), but it is present for all assumptions about parent melts.  
633 The range of Ni variation is comparable to that produced by changes in  $R$  over factors of up to an  
634 order of magnitude.

### 635 Sulfide “cannibalization” and Ni enrichment

636 It is likely that the trapped liquid effect contributes considerably to the “noise” in the data and may  
637 well explain the observation of anomalously Ni rich olivines in some deposits such as Kalatongke,  
638 Savannah, Nova-Bollinger and Kevitsa. However, in a number of cases high Ni is not specifically  
639 associated with sulfide-bearing orthocumulates so another explanation is called for.

640 The sequence of events may be more complex than the simple scenario modelled in Figure 16. For  
641 example, fluid dynamic considerations predict that pools of Ni-enriched magmatic sulfide liquid may  
642 commonly be “cannibalized” and entrained as droplets in a flowing slurry of silicate magma, liquid  
643 sulfide and olivine (Barnes and Robertson, 2019; Lesher, 2019). In this case (Figure 17), we have a  
644 starting scenario similar to Figure 15A, except that rather than starting out as a Ni-free Fe-sulfide  
645 xenomelt, the sulfide component in the slurry is re-entrained magmatic sulfide that already has high  
646 Ni. For example, if the slurry has 5% of sulfide with 10% Ni, 5% olivine with 0.1 % Ni and the silicate  
647 melt has 250 ppm Ni (realistic assumptions for a typical mafic-hosted deposit), the sulfide  
648 component contains 95% of the total Ni budget and will effectively buffer the Ni contents of both  
649 silicate melt and olivine. In contrast, the silicate melt is the predominant reservoir of Fe and Mg and  
650 buffers the olivine Fo content. Where this olivine is relatively Fe-rich, the Fe-Ni exchange reaction  
651 will cause it to gain Ni from the re-entrained sulfide, without greatly affecting the Ni content of that  
652 sulfide component. In a more extreme case, where the sulfide has 30% Ni (towards the upper end of  
653 sulfides associated with komatiites), an olivine with an initial composition of Fo<sub>84</sub> would react  
654 towards a Ni content in excess of 10,000 ppm for a typical Ni/Fe  $K_D$  of around 8, provided that  
655 equilibrium was attained between the three phases during flow. Further trapped liquid reaction

656 post-deposition could then push this value even higher, to the extreme values of 10,000-15,000 ppm  
657 Ni seen in the Ni-PGE ores at Kevitsa. The effect is further amplified as the  $K_D$  value increases with  
658 increasing Ni in the sulfide. This is consistent with the suggestion of Yang et al. (2013) that these  
659 unusual ores could be the result of assimilation of komatiite-derived sulfide, and with the  
660 explanation offered by Burnham et al. (2003) for anomalously Ni-rich olivines in the komatiite-  
661 associated William Lake intrusion in the Thompson Nickel Belt, Manitoba (Burnham et al., 2003).  
662 More generally, the process of re-entrainment of pre-formed magmatic sulfide by magma-olivine  
663 mixtures with variable composition could explain the apparent paradox that several deposits  
664 mentioned above, and also Ntaka Hill (Barnes et al., 2019) and William Lake, show signals of Ni  
665 enrichment rather than depletion in olivine. In particular the presence of a strong Ni enrichment  
666 signal in sulfide-free rocks in the Savannah intrusion (Figure 6B) is attributed to this effect. (It is also  
667 possible that the same effect could operate in reverse: an Mg-rich olivine reacting with sulfide  
668 formed initially in equilibrium with a relatively Mg-poor olivine could have its Ni content reduced).

669 *Figure 17.*

670 Multi-stage emplacement and sulfide re-entrainment in predominantly vertical sill-dyke-conduit  
671 complexes (Barnes et al., 2016) could provide an additional set of confounding factors for the  
672 interpretation of Ni in olivine data. On a more positive note, the presence of anomalously Ni-  
673 enriched olivines within a suite of otherwise similar intrusions may be as much of a positive indicator  
674 for mineralization as depletion.

### 675 **Summary of sources of variation of Ni in olivine.**

676 Multiple sources of variance in Ni content of olivine at given Fo content could be operative at  
677 multiple stages in the formation of a mineral system. Some of these processes are summarized on  
678 Figure 18.

- 679 • Variability in mantle melt composition due to depth, water content (and possibly source).  
680 Baselines for Ni in olivine in relation to Fo content are somewhat lower in orogenic belt  
681 settings relative to intrusions in continental LIPs. This is probably related to differences in  
682 initial parent magma compositions, with plume magmas generally forming deeper and at  
683 higher temperatures (Yao et al., 2018).
- 684 • Subsequent fractional crystallization with and without sulfide (Figure 18);
- 685 • Recharge and magma mixing (Gleeson and Gibson, 2019) (Figure 18);
- 686 • Batch equilibration between olivine and sulfide at variable R and olivine/liquid ratio (Figure  
687 14);



720

## Acknowledgments

721 We thank Yiguan Liu for assistance with data compilation. Data for the Halls Creek Orogen and for  
722 the Nova-Bollinger system were collected within industry funded projects supported by Panoramic  
723 Resources and IGO Ltd respectively. Louise Schoneveld provided a helpful review of a preliminary  
724 draft, and we are grateful to American Mineralogist reviewers James Brenan, Chusi Li and Huan Chen  
725 for constructive suggestions.

726

## Appendices/Supplementary

727 **Supplementary Table 1.** Data source table and references.

### 728 Appendix 1. Modelling methods

729 Mafic-ultramafic magmas in continental LIPs are derived from decompression melting of mantle  
730 beneath the rigid lithosphere. The geochemical characteristics of these mantle-derived magmas are  
731 mostly dependent on geochemical features, mineralogy and potential temperature) of the mantle  
732 source, as well as the melting degree which is determined by the thickness of lithosphere because  
733 the upwelling of mantle ceases at the base of rigid lithosphere. Given that the continental  
734 lithosphere is rarely thinned to below 80-100 km during the LIP event, the representative mantle-  
735 derived magma in the CLIP is adopted as the melt that is generated by the adiabatic decompression  
736 melting of the primary mantle (McDonough and Sun, 1995) with a hot potential temperature  
737 (1550 °C), and extracted from the source at 3 GPa (~100 km). This melt contains ~25 wt% MgO, 14  
738 wt% FeO<sub>t</sub> (total Fe expressed as FeO) and 1040 ppm Ni based on the model from Yao et al. (2018),  
739 and is used for a further model of fractional crystallization at the assumed condition. In order to  
740 account for the effect of mantle heterogeneity, this peridotite-derived melt is also mixed with the  
741 melt generated by a MORB-like pyroxenite mantle with the same decompression melting path  
742 (potential temperature, 1550 °C; terminal melting pressure, 3 GPa). The proportions of pyroxenite-  
743 derived melt in the mixed magmas are assumed as 10, 30 and 50%, respectively. The partition  
744 coefficient of Ni between the olivine and melt is calculated via the new equation that is calibrated on  
745 many 1-bar experiments spanning a wide range of melt and olivine compositions (Pu et al., 2017; Pu  
746 et al., 2021). The partition coefficients of Ni within the clinopyroxene-melt and orthopyroxene-melt  
747 pairs follow the equations from Matzen et al. (2017b). The olivine grains crystallized from the mixed  
748 magmas (especially contain 30-50% pyroxenite-derived melt) contain a higher Ni content than that  
749 of peridotite-derived melt at the high-Fo regime, but all modelled Ni trendlines become overlapped  
750 when the Fo value drops below 78 (Figure 12A). In general, the modelling results coincide with the

751 trends and distributions of CLIP olivine dataset (Fig. 12A) and can be considered as the baseline to  
752 trace the influence of post-cumulus processes on the Ni content of olivines.

753 The petrogenesis of ultramafic-mafic intrusions in orogenic belts is extremely complex, and the  
754 associated magmatism may be generated in subduction, collision and post-collision periods. Hence,  
755 the partial melting process occurred in orogenic belt may involve the flux-melting of mantle wedge  
756 during subduction, the upwelling of asthenosphere due to slab break off or lithospheric  
757 delamination in syn- or post-collisional setting, and even the possible contributions of adiabatic  
758 decompression melting of hot plume material. In the models presented here (Fig. A1), partial  
759 melting processes in orogenic belt are simplified as the flux-melting of mantle wedge above the  
760 subducted slab. The details of this melting model can be found in Yao et al. (2018). The mantle  
761 source is simplified as the depleted MORB mantle (DMM) (Workman and Hart, 2005). We also set a  
762 relatively high temperature (1300 °C) that is close to the anhydrous solidus of mantle wedge  
763 peridotite at the crust-mantle boundary (~ 1 GPa), which corresponds to the subduction of a young  
764 oceanic lithosphere with slow convergence rate and low subduction angle. The melting products  
765 generated at different melting degree (5-25%) are adopted as the representative parental magmas  
766 in orogenic belt to model the subsequent fractional crystallization at 1 kbar pressure. The melts  
767 derived by flux-melting contain the relatively lower Ni contents (~245-273 ppm), and the melting  
768 degrees here show a slight influence on the Ni trendlines of olivine (Figure 12B).

769 *Appendix Figure A1.*

770

## References

- 771 Ariskin, A.A., and Barmina, G.S. (1999) An empirical model for the calculation of spinel-melt  
772 equilibria in mafic igneous systems at atmospheric pressure: 2. Fe-Ti oxides. *Contributions to*  
773 *Mineralogy and Petrology*, 134, 251- 263.
- 774 Ariskin, A.A., Danyushevsky, L.V., Bychkov, K.A., McNeill, A.W., Barmina, G.S., and Nikolaev, G.S.  
775 (2013) Modeling solubility of Fe-Ni sulfides in basaltic magmas: the effect of Ni in the melt.  
776 *Economic Geology*, 108.
- 777 Barnes, S.J. (1986) The effect of trapped liquid crystallization on cumulus mineral compositions in  
778 layered intrusions. *Contributions to Mineralogy and Petrology*, 93, 524-531.
- 779 Barnes, S.J. (2007) Cotectic precipitation of olivine and sulfide liquid from komatiite magma, and the  
780 origin of komatiite-hosted disseminated nickel sulfide mineralization at Mt Keith and  
781 Yakabindie, Western Australia. *Economic Geology*, 102, 299-304.
- 782 Barnes, S.J., Cruden, A.R., Arndt, N.T., and Saumur, B.M. (2016) The mineral system approach  
783 applied to magmatic Ni-Cu-PGE sulphide deposits. *Ore Geology Reviews*, 76, 296-316.
- 784 Barnes, S.J., and Fiorentini, M.L. (2012) Komatiite magmas and nickel sulfide deposits: a comparison  
785 of variably endowed Archean terranes. *Economic Geology*, 107, 755-780.
- 786 Barnes, S.J., Godel, B., Gürer, D., Brenan, J.M., Robertson, J., and Paterson, D. (2013a) Sulfide-olivine  
787 Fe-Ni exchange and the origin of anomalously Ni-rich magmatic sulfides. *Economic Geology*,  
788 108, 1971-1982.
- 789 Barnes, S.J., Heggie, G.J., and Fiorentini, M.L. (2013b) Spatial variation in platinum group element  
790 concentrations in ore-bearing komatiite at the Long-Victor deposit, Kambalda Dome,  
791 Western Australia: enlarging the footprint of nickel sulfide orebodies. *Economic Geology*,  
792 108, 913-933.
- 793 Barnes, S.J., Hill, R.E.T., Perring, C.S., and Dowling, S.E. (2004) Litho-geochemical exploration for  
794 komatiite-associated Ni-sulfide deposits: strategies and limitations. *Mineralogy and*  
795 *Petrology*, 82, 259-293.
- 796 Barnes, S.J., Makkonen, H.V., Dowling, S.E., Hill, R.E.T., and Peltonen, P. (2009) The 1.88 Ga Kotalahti  
797 and Vammala Nickel Belts, Finland: geochemistry of the mafic and ultramafic metavolcanic  
798 rocks. *Bulletin of the Geological Society of Finland*, 81, 103-141.
- 799 Barnes, S.J., Mole, D.R., Hornsey, R., and Schoneveld, L.E. (2019) Nickel-copper sulfide mineralization  
800 in the Ntaka Hill Ultramafic Complex, Nachingwea region, Tanzania. *Economic Geology* 114,  
801 1135-1158.
- 802 Barnes, S.J., and Mungall, J.E. (2018) Blade shaped dykes and nickel sulfide deposits: a model for the  
803 emplacement of ore-bearing small intrusions. *Economic Geology*, 113, 789-798.
- 804 Barnes, S.J., Mungall, J.E., and Maier, W.D. (2015) Platinum group elements in mantle melts and  
805 mantle samples. *Lithos*, 232, 395-417.
- 806 Barnes, S.J., and Naldrett, A.J. (1985) Geochemistry of the JM (Howland) Reef of the Stillwater  
807 Complex, Minneapolis Adit area. I. Sulfide chemistry and sulfide-olivine equilibrium.  
808 *Economic Geology*, 80, 627-645.
- 809 Barnes, S.J., and Robertson, J.C. (2019) Time scales and length scales in magma flow pathways and  
810 the origin of magmatic Ni-Cu-PGE ore deposits. *Geoscience Frontiers*, 10, 77-87.
- 811 Barnes, S.J., Stanley, C.R., and Taranovic, V. (2021) Compositions and Ni-Cu-PGE tenors of Nova-  
812 Bollinger ores with implications for the origin of Pt anomalies in PGE-poor massive sulfides.  
813 *Economic Geology*, in press.
- 814 Barnes, S.J., Taranovic, V., Miller, J.M., Boyce, G., and Beresford, S.W. (2020) Sulfide emplacement  
815 and migration in the Nova-Bollinger Ni-Cu-Co deposit, Albany-Fraser Orogen, Western  
816 Australia. *Economic Geology*, 115, 1749-1776.
- 817 Brenan, J.M., (2003) Effects of  $fO_2$ ,  $fS_2$ , temperature and melt composition on Fe-Ni exchange  
818 between olivine and sulfide liquid: implications for natural olivine-sulfide assemblages .  
819 *Geochimica et Cosmochimica Acta*, 64, 307-320.

- 820 Burnham, O.M., Halden, N., Layton-Matthews, D., Leshner, C.M., Liwanag, J., Heaman, L., Hulbert, L.,  
821 Machado, N., Michalak, D., Pacey, M., Peck, D., Potrel, A., Theyer, P., Toope, K., and Zwanzig,  
822 H. (2003) Geology, Stratigraphy, Petrogenesis, and Metallogenesis of the Thompson Nickel  
823 Belt, Manitoba: Final Report for CAMIRO Project 97E-02, p. 410 pp. Mineral Exploration  
824 Research Centre, Sudbury.
- 825 Campbell, I.H., and Naldrett, A.J. (1979) The influence of silicate:sulphide ratios on the geochemistry  
826 of magmatic sulphides. *Economic Geology*, 74, 1503-1506.
- 827 Clark, T. (1980) Petrology of the Turnagain ultramafic complex, northwestern British Columbia.  
828 *Canadian Journal of Earth Sciences = Revue Canadienne des Sciences de la Terre*, 17(6), 744-  
829 757.
- 830 Deblond, A., and Tack, L. (1999) Main characteristics and review of mineral resources of the  
831 Kabanga-Musongati mafic-ultramafic alignment in Burundi. *Journal of African Earth Sciences*,  
832 29, 313- 328.
- 833 Ding, X., Li, C., Ripley, E.M., Rossell, D., and Kamo, S. (2010) The Eagle and East Eagle sulfide ore-  
834 bearing mafic-ultramafic intrusions in the Midcontinent Rift System, upper Michigan:  
835 Geochronology and petrologic evolution. *Geochemistry, Geophysics, Geosystems*, 11(3).
- 836 Duchesne, J.-C., Liégeois, J.-P., Deblond, A., and Tack, L. (2004) Petrogenesis of the Kabanga-  
837 Musongati layered mafic-ultramafic intrusions in Burundi (Kibaran belt): Geochemical, Sr-  
838 Nd isotopic constraints and Cr-Ni behaviour. *Journal of African Earth Sciences*, 39, 133-145.
- 839 Duke, J.M. (1979) Computer simulation of the fractionation of olivine and sulfide from mafic and  
840 ultramafic magmas. *Canadian Mineralogist*, 76, 507-514.
- 841 Evans, D.M., Boadi, I., Byemelwa, L., Gilligan, J., Kabete, J., and Marcet, P. (2000) Kabanga magmatic  
842 nickel sulphide deposits, Tanzania: Morphology and geo-chemistry of associated intrusions.  
843 *Journal of African Earth Sciences*, 97, 651-674.
- 844 Gao, J.-F., and Zhou, M.-F. (2013) Magma mixing in the genesis of the Kalatongke dioritic intrusion:  
845 Implications for the tectonic switch from subduction to post-collision, Chinese Altay, NW  
846 China. *Lithos*, 162, 236-250.
- 847 Gleeson, M.L.M., and Gibson, S.A. (2019) Crustal controls on apparent mantle pyroxenite signals in  
848 ocean-island basalts. *Geology (Boulder)*, 47(4), 321-324.
- 849 Godel, B., Barnes, S.J., and Barnes, S.-J. (2013) Deposition mechanisms of magmatic sulphide liquids:  
850 evidence from high-resolution X-ray computed tomography and trace element chemistry of  
851 komatiite-hosted disseminated sulphides. *Journal of Petrology*, 54, 1455-1481.
- 852 Häkli, T.A. (1971) Silicate nickel and its application to the exploration of nickel ores. *Bulletin of the*  
853 *Geological Society of Finland*, 43, 247-263.
- 854 Hart, S.R., and Davis, K.E. (1978) Ni partitioning between olivine and silicate melt. *Earth and*  
855 *Planetary Science Letters*, 40, 203-219.
- 856 Helmy, H.M., and Mogessie, A. (2001) Gabbro Akarem, Eastern Desert, Egypt; Cu-Ni-PGE  
857 mineralization in a concentrically zoned mafic-ultramafic complex. *Mineralium Deposita*,  
858 36(1), 58-71.
- 859 Herzberg, C., Vidito, C., and Starkey, N.A. (2016) Nickel-cobalt contents of olivine record origins of  
860 mantle peridotite and related rocks. *The American Mineralogist*, 101(9), 1952-1966.
- 861 Jesus, A., Mateus, A., Benoit, M., Tassinari, C., and Bento dos Santos, T. (2020) The timing of sulfide  
862 segregation in a Variscan synorogenic gabbroic layered intrusion (Beja, Portugal):  
863 Implications for Ni-Cu-PGE exploration in orogenic settings. *Ore Geology Reviews*.
- 864 Jugo, P.J., Luth, R.W., and Richards, J.P. (2005) Experimental data on the speciation of sulfur as a  
865 function of oxygen fugacity in basaltic melts. *Geochimica et Cosmochimica Acta*, 69(2), 497-  
866 503.
- 867 Kiseeva, E.S., and Wood, B.J. (2015) The effects of composition and temperature on chalcophile and  
868 lithophile element partitioning into magmatic sulphides. *Earth and Planetary Science Letters*,  
869 424, 280-294.

- 870 Kohanpour, F., Górczyk, W., Lindsay, M.D., and Occhipinti, S.A. (2017) Examining tectonic scenarios  
871 using geodynamic numerical modelling: Halls Creek Orogen, Australia. *Gondwana Research*,  
872 46, 95-113.
- 873 Lamberg, P. (2005) From genetic concepts to practice – lithogeochemical identification of Ni-Cu  
874 mineralised intrusions and localization of the ore. *Geological Survey of Finland Bulletin*, 402,  
875 1-266.
- 876 Le Vaillant, M., Barnes, S.J., Mole, D.R., Fiorentini, M.L., LaFlamme, C.K., Denyszyn, S., Austin, J.,  
877 Patterson, B., Godel, B., Neaud, A., Hicks, J., Shaw-Stuart, A., and Mao, Y.J. (2020)  
878 Multidisciplinary study of a complex magmatic system: The Savannah Ni-Cu-Co Camp,  
879 Western Australia. *Ore Geology Reviews*, 117, 103292.
- 880 Le Vaillant, M., Fiorentini, M.L., and Barnes, S.J. (2016) Review of lithogeochemical exploration tools  
881 for komatiite-hosted nickel sulphide deposits. *Journal of Geochemical Exploration*, 168, 1-19.
- 882 Le Vaillant, M., Hill, E.J., and Barnes, S.J. (2017) Simplifying drill-hole domains for 3D geochemical  
883 modelling: an example from the Kevitsa Ni-Cu-(PGE) deposit. *Ore Geology Reviews*, 90, 388-  
884 398.
- 885 Lehnert, K., Su, Y., Langmuir, C.H., Sarbas, B., and Nohl, U. (2000) A global geochemical database  
886 structure for rocks. *Geochemistry Geophysics Geosystems*, 1, 1012.
- 887 Leshner, C.M. (2017) Roles of residues/skarns, xenoliths, xenocrysts, xenomelts, and xenovolatiles in  
888 the genesis, transport, and localization of magmatic Fe-Ni-Cu-PGE sulfides and chromite. *Ore*  
889 *Geology Reviews*, 90, 465-484.
- 890 Leshner, C.M. (2019) Up, down, or sideways: emplacement of magmatic Fe–Ni–Cu–PGE sulfide melts  
891 in large igneous provinces. *Canadian Journal of Earth Science*, 56, 756-773.
- 892 Li, C., and Naldrett, A.J. (1999) Geology and petrology of the Voisey's Bay intrusion: reaction of  
893 olivine with sulfide and silicate liquids. *Lithos*, 47, 1- 31.
- 894 Li, C., Naldrett, A.J., and Ripley, E.M. (2007) Controls on the Fo and Ni Contents of Olivine in Sulfide-  
895 bearing Mafic/Ultramafic Intrusions: Principles, Modeling, and Examples from Voisey's Bay.  
896 *Earth Science Frontiers*, 14, 177-183.
- 897 Li, C., Ripley, E.M., Thakurta, J., Stifter, E.C., and Liang, Q. (2013) Variations of olivine Fo-Ni contents  
898 and highly chalcophile element abundances in arc ultramafic cumulates, southern Alaska.  
899 *Chemical Geology*, 351, 15-28.
- 900 Li, C., Zhang, M., Fu, P., Qian, Z.Z., Hu, P., and Ripley, E.M. (2012) The Kalatongke magmatic Ni-Cu  
901 deposits in the Central Asian Orogenic Belt, NW China: product of slab window magmatism?  
902 *Mineralium Deposita*, 47(1-2), 51-67.
- 903 Li, C., Zhang, Z., Li, W., Wang, Y., Sun, T., and Ripley, E.M. (2015) Geochronology, petrology and Hf-S  
904 isotope geochemistry of the newly-discovered Xiarihamu magmatic Ni-Cu sulfide deposit in  
905 the Qinghai-Tibet Plateau, western China. *Lithos (Oslo)*, 216-217, 224-240.
- 906 Li, C.S., and Ripley, E.M. (2005) Empirical equations to predict the sulfur content of mafic magmas at  
907 sulfide saturation and applications to magmatic sulfide deposits. *Mineralium Deposita*, 40,  
908 218-230.
- 909 Li, C.S., and Ripley, E.M. (2010) The relative effects of composition and temperature on olivine-liquid  
910 Ni partitioning: Statistical deconvolution and implications for petrologic modeling. *Chemical*  
911 *Geology*, 275(1-2), 99-104.
- 912 Lu, Y., Leshner, C.M., and Deng, J. (2019) Geochemistry and genesis of magmatic Ni-Cu-(PGE) and  
913 PGE-(Cu)-(Ni) deposits in China. *Ore Geology Reviews*, 107, 863-887.
- 914 Luolavirta, K., Hanski, E., Maier, W., Lahaye, Y., O'Brien, H., and Santaguida, F. (2018) In situ  
915 strontium and sulfur isotope investigation of the Ni-Cu-(PGE) sulfide ore-bearing Kevitsa  
916 Intrusion, northern Finland. *Mineralium Deposita*, 53(7), 1019-1038.
- 917 Luolavirta, K., Hanski, E., Maier, W., and Santaguida, F. (2017) Whole-rock and mineral compositional  
918 constraints on the magmatic evolution of the Ni-Cu-(PGE) sulfide ore-bearing Kevitsa  
919 intrusion, northern Finland. *Lithos*, 296-299, 37-53.

- 920 Maier, W.D., Barnes, S.-J., and Groves, D.I. (2013) The Bushveld Complex, South Africa; formation of  
921 platinum-palladium, chrome- and vanadium-rich layers via hydrodynamic sorting of a  
922 mobilized cumulate slurry in a large, relatively slowly cooling, subsiding magma chamber.  
923 *Mineralium Deposita*, 48(1), 1-56.
- 924 Maier, W.D., Barnes, S.-J., and Ripley, E.M. (2011) The Kabanga Ni Sulfide Deposits, Tanzania: A  
925 Review of Ore-Forming Processes. *Reviews in Economic Geology*, 17, 217-234.
- 926 Maier, W.D., Barnes, S.J., Sarkar, A., Ripley, E.M., Li, C., and Livesey, T. (2010) The Kabanga Ni sulfide  
927 deposit, Tanzania: I. Geology, petrography, silicate rock geochemistry, and sulfur and oxygen  
928 isotopes. *Mineralium Deposita*, 45, 419-441.
- 929 Maier, W.D., Peltonen, P., and Livesey, T. (2007) The ages of the Kabanga north and Kapalagulu  
930 intrusions, western Tanzania: A reconnaissance study. *Economic Geology*, 102, 147-149.
- 931 Maier, W.D., Smithies, R.H., Spaggiari, C.V., Barnes, S.J., Kirkland, C.L., Yang, S., Lahaye, Y., Kiddie, O.,  
932 and MacRae, C.M. (2016) Petrogenesis and Ni-Cu sulphide potential of mafic-ultramafic  
933 rocks in the Mesoproterozoic Fraser Zone within the Albany-Fraser Orogen, Western  
934 Australia. *Precambrian Research*, 281, 27-46.
- 935 Mäkitie, H., Data, G., Isabirye, E., Mänttari, I., Huhma, H., Klausen, M.B., Pakkanen, L., and  
936 Virransalo, P. (2014) Petrology, geochronology and emplacement model of the giant 1.37 Ga  
937 arcuate Lake Victoria dyke swarm on the margin of a large igneous province in eastern  
938 Africa. *Journal of African Earth Sciences*, 97, 273– 296.
- 939 Makkonen, H.V. (2015) Nickel deposits of the 1.88 Ga Kotalahti and Vammala Belts. In W.D. Maier, R.  
940 Lahtinen, and H. O' Brien, Eds. *Mineral Deposits of Finland*, p. 253-287. Elsevier.
- 941 Makkonen, H.V., Makinen, J., and Kontoniemi, O. (2008) Geochemical discrimination between  
942 barren and mineralized intrusions in the Svecofennian (1.9 Ga) Kotalahti nickel belt, Finland.  
943 *Ore Geology Reviews*, 33(1), 101-114.
- 944 Mao, J.W., Pirajno, F., Zhang, Z.H., Chai, F.M., Wu, H., Chen, S.P., Cheng, L.S., Yang, J.M., and Zhang,  
945 C.Q. (2008) A review of the Cu-Ni sulphide deposits in the Chinese Tianshan and Altay  
946 orogens (Xinjiang Autonomous Region, NW China): Principal characteristics and ore-forming  
947 processes. *Journal of Asian Earth Sciences*, 32(2-4), 184-203.
- 948 Mao, Y.J., Barnes, S.J., Godel, B., Schoneveld, L.E., Qin, K.Z., Tang, D.M., Williams, M.J., and Kang, Z.  
949 (2021) Sulfide ore formation of the Kalatongke Ni-Cu deposit as illustrated by sulfide  
950 textures. *Economic Geology*, in revision.
- 951 Mao, Y.J., Qin, K.Z., Barnes, S.J., Ferraina, C., Iacono-Marziano, G., Verrall, M.R., Tang, D.M., and Xue,  
952 S.C. (2017) A revised oxygen barometry in sulfide-saturated magmas and application to the  
953 Permian magmatic Ni–Cu deposits in the southern Central Asian Orogenic Belt. *Mineralium  
954 Deposita*, 53, 731-755.
- 955 Matzen, A.K., Baker, M.B., Beckett, J.R., and Stolper, E.M. (2013) The temperature and pressure  
956 dependence of nickel partitioning between olivine and silicate melt. *Journal of Petrology*, 54,  
957 2521-2545.
- 958 Matzen, A.K., Baker, M.B., Beckett, J.R., Wood, B.J., and Stolper, E.M. (2017a) The effect of liquid  
959 composition on the partitioning of Ni between olivine and silicate melt. *Contributions to  
960 Mineralogy and Petrology*, 172(1), 3.
- 961 Matzen, A.K., Wood, B.J., Baker, M.B., and Stolper, E.M. (2017b) The roles of pyroxenite and  
962 peridotite in the mantle sources of oceanic basalts. *Nature Geoscience*, 10(7), 530-535.
- 963 McDonough, W.F., and Sun, S.-S. (1995) The composition of the Earth. *Chemical Geology*, 120, 223-  
964 253.
- 965 Mole, D.R., Barnes, S.J., Le Vaillant, M., Martin, L.A.J., and Hick, J. (2018) Timing, geochemistry and  
966 tectonic setting of intrusion-hosted Ni-Cu sulfide deposits of the Halls Creek Orogen,  
967 Western Australia. *Lithos*, 314-315, 425-446.
- 968 Mutanen, T. (1997) Geology and ore petrology of the Akanvaara and Koitelainen mafic layered  
969 intrusions and the Keivitsa-Satovaa layered complex, northern Finland. *Bulletin of the  
970 Geological Survey of Finland*, 395.

- 971 Naldrett, A.J., Duke, J.M., Lightfoot, P.C., and Thompson, J.F.H. (1984) Quantitative modelling of the  
972 segregation of magmatic sulphides: an exploration guide. Canadian Institute of Mining and  
973 Metallurgy Bulletin, 77, 46-56.
- 974 Pu, X., Lange, R.A., and Moore, G. (2017) A comparison of olivine-melt thermometers based on D  
975 (sub Mg) and D (sub Ni) ; the effects of melt composition, temperature, and pressure with  
976 applications to MORBs and hydrous arc basalts. American Mineralogist, 102(4), 750-765.
- 977 Pu, X., Moore, G.M., Lange, R.A., Touran, J.P., and Gagnon, J.E. (2021) Experimental evaluation of a  
978 new H (sub 2) O-independent thermometer based on olivine-melt Ni partitioning at crustal  
979 pressure. American Mineralogist, 106(2), 235-250.
- 980 Qin, K.-Z., Su, B.-X., Sakyi, P.A., Tang, D.M., Li, X.H., Sun, H., Xiao, Q.H., and Liu, P.P. (2011) Sims  
981 zircon U-Pb geochronology and Sr-Nd isotopes of Ni-Cu-bearing mafic-ultramafic intrusions  
982 in Eastern tianshan and Beishan in correlation with flood basalts in Tarim basin (NW china):  
983 Constraints on a Ca. 280 Ma mantle plume. American Journal of Science, 311(3), 237-260.
- 984 Santaguida, F., Luolavirta, K., Lappalainen, M., Ylinen, J., Voipio, S., and Jones, S. (2015) The Kevitsa  
985 Ni-Cu-PGE deposit in the Central Lapland Greenstone Belt in Finland. In W.D. Maier, R.  
986 Lahtinen, and H. O' Brien, Eds. Mineral Deposits of Finland, p. 195-210. Elsevier.
- 987 Sarbas, B. (2008) The GEOROC database as part of a growing geoinformatics network. In S.R. Brady,  
988 A.K. Sinha, and L.C. Gunderson, Eds. Geoinformatics 2008 - data to knowledge, Proceedings.  
989 US Geological Survey Scientific Investigations Report 2008-5172, p. 42-43.
- 990 Savov, I.P., Ryan, J.G., D'Antonio, M., and Fryer, P. (2007) Shallow slab fluid release across and along  
991 the Mariana arc-basin system; insights from geochemistry of serpentinized peridotites from  
992 the Mariana fore arc. Journal of Geophysical Research, 112(B9), B09205.
- 993 Schoneveld, L.E., Barnes, S.J., Makkonen, H.V., Le Vaillant, M., Paterson, D.J., Taranovic, V., Wang, K.-  
994 Y., and Mao, Y.-J. (2020) Zoned Pyroxenes as Prospectivity Indicators for Magmatic Ni-Cu  
995 Sulfide Mineralization. Frontiers in Earth Science, 8(256).
- 996 Sobolev, A., Hoffman, A., Kuzmin, D., Yaxley, G., Arndt, N., Chung, S.-L., Danyushevsky, L., Elliott, T.,  
997 Frey, F., Garcia, M., Gurenko, A., Kamenetsky, V., Kerr, A., Krivolutsкая, N., Matvienkov, V.,  
998 Nikogosian, I., Rocholl, A., Sigurdson, I., Sushchevskaya, N., and Teklay, M. (2007) The  
999 amount of recycled crust in sources of mantle-derived melts. Science, 316, 412-417.
- 1000 Sobolev, A.V., Hofmann, A.W., Sobolev, S.V., and Nikogosian, I.K. (2005) An olivine-free mantle  
1001 source of Hawaiian shield basalts. Nature (London), 434(7033), 590.
- 1002 Song, X.-Y., Xie, W., Deng, Y.-F., Crawford, A.J., Zheng, W.-Q., Zhou, G.-F., Deng, G., Cheng, S.-L., and  
1003 Li, J. (2011a) Slab break-off and the formation of Permian mafic-ultramafic intrusions in  
1004 southern margin of Central Asian Orogenic Belt, Xinjiang, NW China. Lithos, 127(1-2), 128-  
1005 143.
- 1006 Song, X., Wang, Y., and Chen, L. (2011b) Magmatic Ni-Cu-(PGE) deposits in magma plumbing  
1007 systems; features, formation and exploration. Geoscience Frontiers, 2(3), 375-384.
- 1008 Song, X., Xie, W., Deng, Y., Crawford, A.J., Zheng, W., Zhou, G., Deng, G., Cheng, S., and Li, J. (2011c)  
1009 Slab break-off and the formation of Permian mafic-ultramafic intrusions in southern margin  
1010 of Central Asian orogenic belt, Xinjiang, NW China. Lithos (Oslo), 127(1-2), 128-143.
- 1011 Song, X., Yi, J., Chen, L., She, Y., Liu, C., Dang, X., Yang, Q., and Wu, S. (2016) The giant Xiarihamu Ni-  
1012 Co sulfide deposit in the East Kunlun orogenic belt, northern Tibet Plateau, China. Economic  
1013 Geology and the Bulletin of the Society of Economic Geologists, 111(1), 29-55.
- 1014 Song, X.Y., Wang, K.Y., Barnes, S.J., Yi, J.-N., and Schoneveld, L.E. (2020) Petrogenetic insights of  
1015 chromite in ultramafic cumulates: Implications from the Xiarihamu intrusion, northern Tibet  
1016 Plateau, China. American Mineralogist, 105, 479-497.
- 1017 Spaggiari, C.V., Kirkland, C.L., Smithies, R.H., Wingate, M.T.D., and Belousova, E. (2015)  
1018 Transformation of an Archean craton margin during Proterozoic basin formation and  
1019 magmatism: the Albany-Fraser Orogen, Western Australia. Precambrian Research, 266, 440-  
1020 466.

- 1021 Su, B.-X., Qin, K.-Z., Sakyi, P.A., Li, X.-H., Yang, Y.-H., Sun, H., Tang, D.-M., Liu, P.-P., Xiao, Q.-H., and  
1022 Malaviarachchi, S.P.K. (2011) U–Pb ages and Hf–O isotopes of zircons from Late Paleozoic  
1023 mafic–ultramafic units in the southern Central Asian Orogenic Belt: Tectonic implications  
1024 and evidence for an Early-Permian mantle plume. *Gondwana Research*, 20(2-3), 516-531.
- 1025 Taranovic, V., Barnes, S.J., Beresford, S.W., Williams, M.J., MacRae, C., and Schoneveld, L.E. (2021)  
1026 Nova – Bollinger Ni – Cu Sulfide Ore Deposits, Fraser Zone, Western Australia: Petrogenesis  
1027 of the Host Intrusions. *Economic Geology*, in press.
- 1028 Thakurta, J., Ripley, E.M., and Li, C. (2014) Platinum group element geochemistry of sulfide-rich  
1029 horizons in the Ural-Alaskan-type ultramafic complex of Duke Island, southeastern Alaska.  
1030 *Economic Geology and the Bulletin of the Society of Economic Geologists*, 109(3), 643-659.
- 1031 Thakurta, J., Ripley, E.M., and Li, C.S. (2008) Pre-requisites for Sulphide-poor PGE and Sulphide-rich  
1032 Cu-Ni-PGE Mineralization in Alaskan-type Complexes. *Journal of the Geological Society of  
1033 India*, 72(5), 611-622.
- 1034 Wei, B., Wang, C.Y., Li, C., and Sun, Y. (2013) Origin of PGE-Depleted Ni-Cu Sulfide Mineralization in  
1035 the Triassic Hongqiling No. 7 Orthopyroxenite Intrusion, Central Asian Orogenic Belt,  
1036 Northeastern China. *Economic Geology*, 108(8), 1813-1831.
- 1037 Workman, R.K., and Hart, S.R. (2005) Major and trace element composition of the depleted MORB  
1038 mantle (DMM). *Earth and Planetary Science Letters*, 231(1-2), 53-72.
- 1039 Xue, S., Qin, K., Li, C., Tang, D., Mao, Y.-J., and Qi L. (2016) Geochronological, Petrological, and  
1040 Geochemical Constraints on Ni-Cu Sulfide Mineralization in the Poyi Ultramafic-Troctolitic  
1041 Intrusion in the Northeast Rim of the Tarim Craton, Western China. *Economic Geology*, 111,  
1042 1465-1484.
- 1043 Yang, S.-H., Maier, W.D., Hanski, E.J., Lappalainen, M., Santaguida, F., and Maatta, S. (2013) Origin of  
1044 ultra-nickeliferous olivine in the Kevitsa Ni-Cu-PGE-mineralized intrusion, northern Finland.  
1045 *Contributions to Mineralogy and Petrology*, 166(1), 81-95.
- 1046 Yao, Z.-s., and Mungall, J.E. (2021) Linking the Siberian Flood Basalts and Giant Ni-Cu-PGE Sulfide  
1047 Deposits at Norilsk. *Journal of Geophysical Research: Solid Earth*, 126(3), e2020JB020823.
- 1048 Yao, Z., Qin, K.Z., and Mungall, E. (2018) Tectonic controls on Ni and Cu contents of primary mantle-  
1049 derived magmas for the formation of magmatic sulfide deposits. *American Mineralogist*,  
1050 online AM-18-106392.
- 1051 Zhang, M., Li, C., Fu, P., Hu, P., and Ripley, E. (2011) The Permian Huangshanxi Cu–Ni deposit in  
1052 western China: intrusive–extrusive association, ore genesis, and exploration implications.  
1053 *Mineralium Deposita*, 46(2), 153-170.
- 1054 Zhang, Z.C., Ma, J.W., Wang, F.S., Hao, Y.L., and Mahoney, J.J. (2005) Mantle Plume Activity and  
1055 Melting Conditions: Evidence From Olivines in Picritic-Komatiitic Rocks From the Emeishan  
1056 Large Igneous Province, Southwestern China. *Episodes*, 28(3), 171-176.
- 1057 Zhang, Z.C., Mao, J.W., Chai, F.M., Yan, S.H., Chen, B.L., and Pirajno, F. (2009) Geochemistry of the  
1058 Permian Kalatongke Mafic Intrusions, Northern Xinjiang, Northwest China: Implications for  
1059 the Genesis of Magmatic Ni-Cu Sulfide Deposits. *Economic Geology*, 104(2), 185-203.
- 1060
- 1061

1062 **Figure captions**

1063 Figure 1 Sobolev et al. (2008) and GEOROC basaltic olivine data set. A, Sobolev data, for continental  
1064 and oceanic LIPs (CLIP, OLIP) and MORB. B, Sobolev CLIP data, excluding the outlying Gudchichinsky  
1065 Picrites (Siberia) with 90th and 50th percentile data density contours. C Density shaded data cloud  
1066 for Oceanic LIPs only (individual points are 95th percentile outliers) shown over the CLIP contours  
1067 and with 90th percentile data contour on MORB olivines. D, Comparison of convergent margin data:  
1068 data points are olivines from GEOROC data compilation for tholeiitic and picritic  
1069 volcanic/subvolcanic rocks from continental (pink) and oceanic (green) convergent margin settings  
1070 including active arcs, compared with Sobolev CLIP data density fields (grey).

1071 Figure 2. Comparison of olivine from unmineralized intrusions, small intrusions and large LMIs  
1072 combined, between LIP settings (A – 550 data points) and orogenic belt settings (B – 844 data  
1073 points), both showing data points and contoured data density. A shows data points for LIP intrusions  
1074 over outline for CLIP basalts from Sobolev et al. (Figure 1), B shows orogenic belt intrusions over  
1075 50th and 90th density contours for barren LIP intrusions. Field labelled MSFM is for olivines formed  
1076 as fractional crystallization products of modelled sulfide-free mantle melts, based on computational  
1077 modelling described in detail below.

1078 Figure 3. Proterozoic plus Phanerozoic CLIP-LMI settings. A, Data points for mineralized intrusions  
1079 over cloud for barren intrusions from Figure 2A. B, same dataset, mineralized only, subdivided by  
1080 locality. Note that scale is trimmed to exclude extreme Ni enriched olivines from Kevitsa discussed  
1081 below. In this and most following plots, red symbols indicate Mineralized, green indicated  
1082 Disseminated or minor mineralization – see Methods section for definitions. Curve labelled MSFM is  
1083 modelled outline for olivines derived from variably fractionated model sulfide free mantle melts  
1084 (MSFM). Grey fields are data cloud for unmineralized LIP-related intrusions.

1085 Figure 4. Orogenic belt settings – Proterozoic (A) + Phanerozoic (B). Data points for mineralized  
1086 intrusions over cloud (yellow) for barren orogenic belt intrusions from Figure 2B and modelled  
1087 outline for olivines derived from variably fractionated model sulfide free mantle melts (MSFM).  
1088 CAOB = Central Asia Orogenic Belt in China; ACO = Appalachian-Caledonian Orogen; KBF = Kotalahti  
1089 Belt (Svecofennian Orogen), Finland.

1090 Figure 5. Ni-Fo plot for samples from the Kabanga–Musongati–Kapalagulu Belt. Contours on data  
1091 densities for barren intrusions from CLIP and LMI grouping.

1092 Figure 6. A) Olivines from the Sally Malay suite of intrusions in the Halls Creek Orogen, over data  
1093 cloud for barren intrusions from orogenic belts (yellow). Savannah, Savannah North and Copernicus

1094 host the known economic deposits, Dave Hill and Wilsons contain sparse localized disseminated  
1095 sulfides. MSFM is theoretical range for olivines from sulfide-free mantle melts. B) Same data set,  
1096 coloured by sulfide content of individual samples – B= barren (no visible sulfide, and/or less than  
1097 0.1% S), D=containing disseminated sulfide.

1098 Figure 7. A, Olivines from small intrusions in the Central Asian Orogenic Belt in NW China and the  
1099 Xiarihamu intrusion, Tibet. All intrusions are mineralized to varying degrees. Field for data from  
1100 barren intrusions from orogenic belts (Figure 2). MSFM is model field for sulfide-free olivines from  
1101 mantle melts. Note that: “Beishan” here represents a summary of the olivine data from the mafic-  
1102 ultramafic intrusions located in the Beishan area, except the Poyi intrusion; the olivine data of  
1103 Honqiling and Tulaergen deposits is collected from the disseminated mineralization. B, Same data  
1104 set excluding Xiarihamu, subdivided by sulfide content of sample (B = <100 ppm Cu, D = >100 ppm  
1105 Cu).

1106 Figure 8. Ni vs Fo plot of olivines from intrusions in the Svecofennian (Kotalahti) Belt of central  
1107 Finland. Contours are on data from barren intrusions in orogenic settings. MSFM is model field for  
1108 sulfide-free olivines from mantle melts.

1109 Figure 9. Ural-Alaskan Type Complexes. MSFM is model field for sulfide-free olivines from mantle  
1110 melts.

1111 Figure 10. Olivine compositions from the Kevitsa intrusion. Ni-PGE = High Ni-PGE tenor orezone, Ni  
1112 tenors up to 30%. A, all data, subdivided by ore type. Xenolith is a sample of an ultramafic xenolith  
1113 within this zone. “Normal” includes disseminated ores with a wide range of Ni tenors. Most Ni  
1114 depleted samples are from zones of “False Ore”, pyrrhotite-rich disseminated sulfides associated  
1115 with country rock metasediment xenoliths. Ni-PGE ores are defined on the basis of high Ni and PGE  
1116 tenors in sulfide (Yang et al., 2013). B, Ni-PGE ore type only, data subdivided by sample for all  
1117 samples with >6 individual spot analyses. Note the strong negative correlation between Ni and Fo  
1118 content within samples. MSFM is model field for sulfide-free olivines from mantle melts.

1119 Figure 11. Olivine compositions in the Nova-Bollinger system. A, Ni vs Fo plot, shapes indicate host  
1120 intrusion, colours are arbitrary indications of range of Ni-Fo. Fields for barren orogenic belt  
1121 intrusions (yellow) and 90th percentile outline for barren LIP intrusions (grey dashed lines). Arrows  
1122 indicate locations of different composition types on (B), projected long section in vertical plane,  
1123 looking north, through entire system. Note the most Ni-depleted Fo rich olivines are located within  
1124 the upper part of the Upper Intrusion, more Fe rich with trends towards Ni enriched olivine are in  
1125 the Lower (ore-bearing) intrusion.

1126 Figure 12 – model curves for olivine compositions generated by low-pressure fractional  
1127 crystallization from various starting magmas (see Appendix)

1128 Figure 13 Low-pressure fractional crystallization (FC) trends for the indicated pressure,  $fO_2$  and  
1129 magma water content. The proportion ratios of olivine and sulfide in each crystallization increment  
1130 are assumed as 50, 100, 200 and 500. The partition coefficient of Ni between sulfide and melt is  
1131 calculated by the recent comprehensive model from Kiseeva and Wood (2015). In (B), the mantle  
1132 source in flux melting is assumed to enrich in Ni (~3050 ppm), because the slab-metasomatized  
1133 mantle wedge can show extreme enrichment of Ni and fluid mobile elements (Savov et al., 2007).

1134 Figure 14. Model single-stage batch equilibrium calculations for olivine and sulfide Ni contents as a  
1135 function of silicate melt/sulfide melt mass ratio R factor for the four idealized silicate melt  
1136 compositions indicated in Table 1. Sulfide equilibrates with mixture of 95% silicate melt, 5% olivine.  
1137 See Barnes et al. (2013) for details of calculation procedure.

1138 Figure 15. Cartoon of olivine-trapped liquid reaction. A. Flowing slurry of silicate + sulfide melts and  
1139 olivine. B, accumulation of olivine, sulfide in different proportions to form a cumulate mush with  
1140 ~40% silicate melt. Phases assumed to have the same compositions as A. C, cooling and equilibrium  
1141 crystallization of the trapped intercumulus liquid causes olivine to evolve towards more Fe rich  
1142 composition, hence also becoming more Ni rich due the Fe-Ni exchange reaction (equns. 1,2).

1143 Figure 16. Calculation showing theoretical effect of trapped liquid equilibration in olivine-sulfide  
1144 orthocumulates (olivine-plagioclase orthocumulate in the basaltic case) with 5% modal % sulfide, for  
1145 various silicate liquid compositions. Dash lines join points for the same R factor. “Original”  
1146 compositions, corresponding to stage A in Figure 15, are olivines in equilibrium with sulfide and  
1147 silicate liquid (95% liquid, 5% olivine) for different values of R and different starting silicate melt  
1148 compositions (Table 1) corresponding to komatiite with 30% MgO, plume “picrite” basalt with 18%  
1149 MgO, Ferropicrite with 14% MgO and MORB basalt (8% MgO), all being representative  
1150 compositions from the modelling results described above. Note that a larger shift in olivine Fo is  
1151 assumed for the cumulate from the low-Mg mafic magma owing to a lower modal proportion of  
1152 olivine in the cumulus assemblage – see Barnes (1986).

1153 Figure 17. Model for generation of Ni-enriched olivine by “cannibalization” of previously formed  
1154 sulfide. A, initial formation of Ni-rich sulfide liquid pool from an Mg-rich magma. B, flushing of flow  
1155 pathway by more evolved magma carrying relatively low-Fo, Fe-enriched olivine. Reaction of this  
1156 olivine with stage-A Ni-rich sulfide causes Ni content of olivine to increase due to the Fe-Ni exchange  
1157 reaction (equation 1).

1158 Figure 18. Schematic diagram showing the multiple factors influencing final olivine compositions.  
 1159 Single dashed lines indicate olivine-only fractional crystallization (FX) from idealized primitive mantle  
 1160 melts from deep plume source and from flux melting of hydrated mantle. FX(ol-sul) indicates effect  
 1161 of fractional crystallization/liquation of a cotectic olivine-sulfide assemblage from primitive plume  
 1162 melt. TL = effect of re-equilibration during solidification of trapped intercumulus liquid, with and  
 1163 without presence of cumulus sulfide. Recharge and mixing indicates effect of mixing fractionated  
 1164 and primitive magmas (Gleeson & Gibson, 2019). Batch sulfide extraction indicates effect of addition  
 1165 of xenomelt sulfide and batch equilibration with melt and olivine (Figure 14).

1166 Appendix Figure A1. The influences of crystallization environments (A. crystallization pressure; B.  
 1167 initial H<sub>2</sub>O content; and C-D. oxygen fugacity) on the Ni contents of olivine grains that are  
 1168 crystallized from parental magma derived by the adiabatic decompression melting in plume (A-C)  
 1169 and the flux melting of DMM in subduction zone (D).

1170

1171 Table 1.

1172 Starting compositions for batch equilibrium - trapped liquid reaction model in Figure 16. (eqm)  
 1173 indicates composition of olivine or sulfide liquid at R>10,000

	Kom	Plume bas 18	Ferropicrite 14	MORB 8
Ni sil	1600	660	350	100
FeOsil	10.0	12	14.0	8.5
MgOsil	30.0	18.0	14.0	8.0
Cu sil	50	100	100	200
NiOl (eqm)	3191	3430	2444	1505
FoOl (eqm)	93.8	88.8	84.4	85.4
Sul liq (eqm)	37.9	24.9	13.6	6.9
T	1600	1380	1280	1140

1174

1175

fig 1

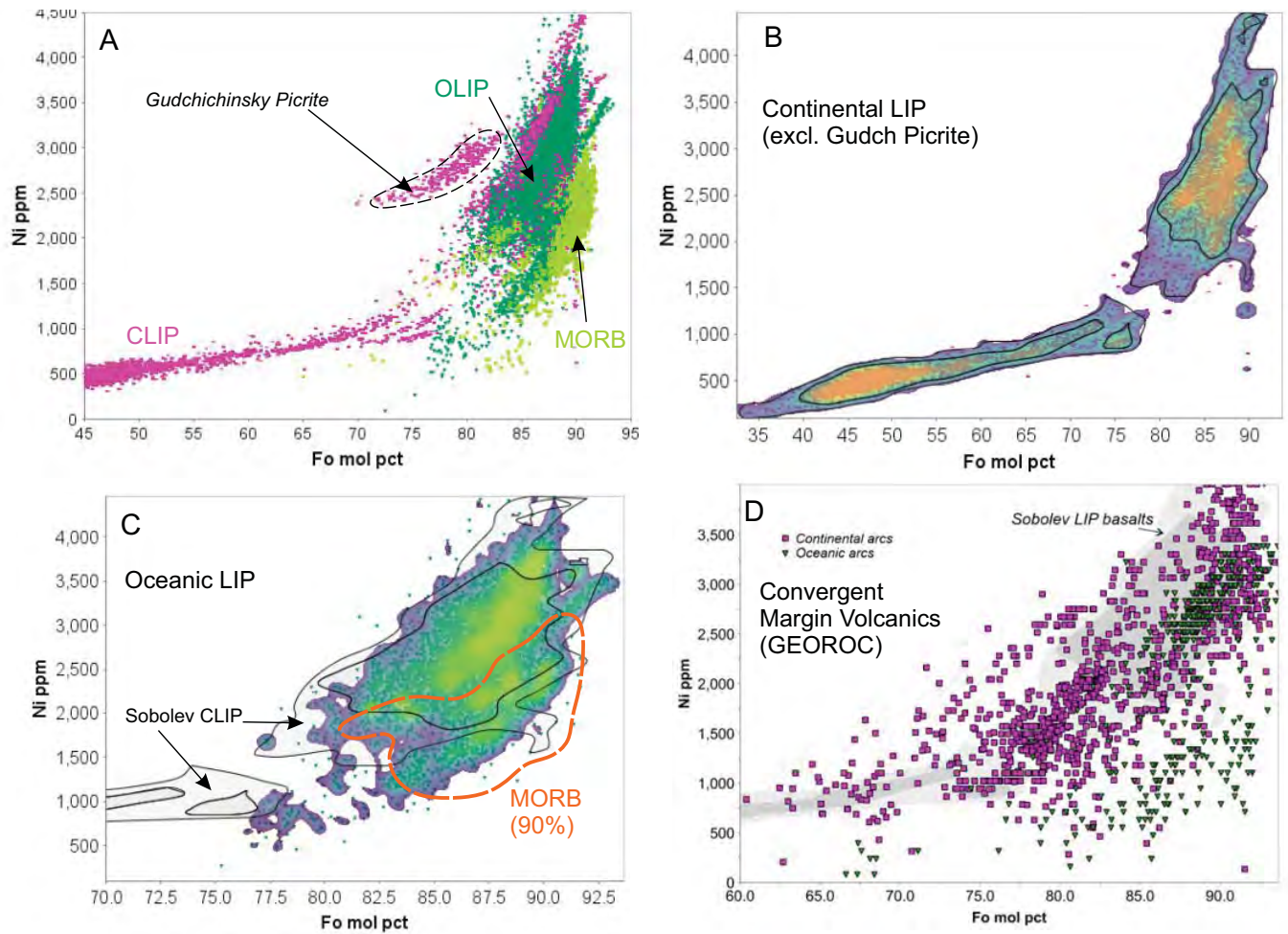


fig 2

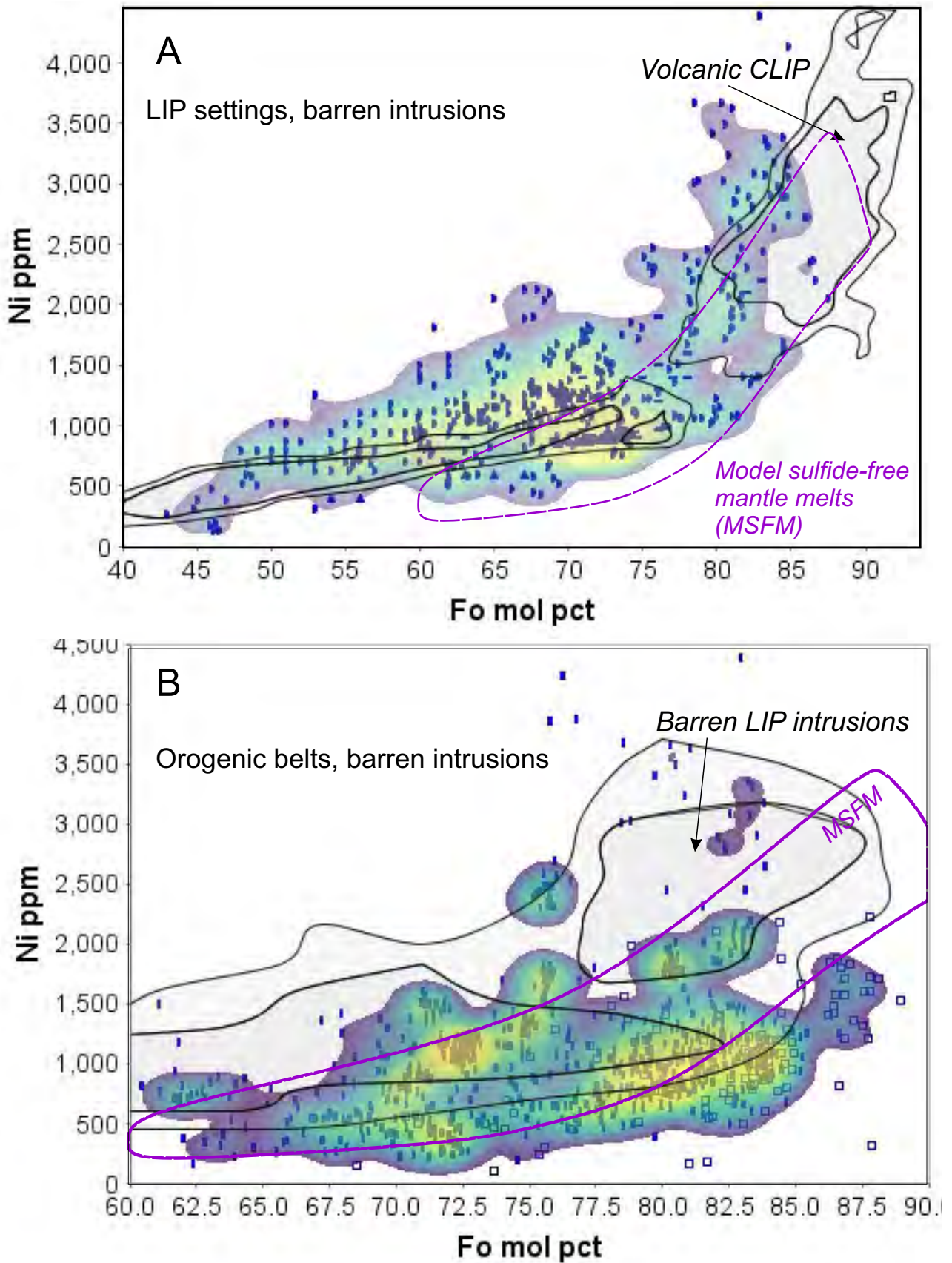


fig 3

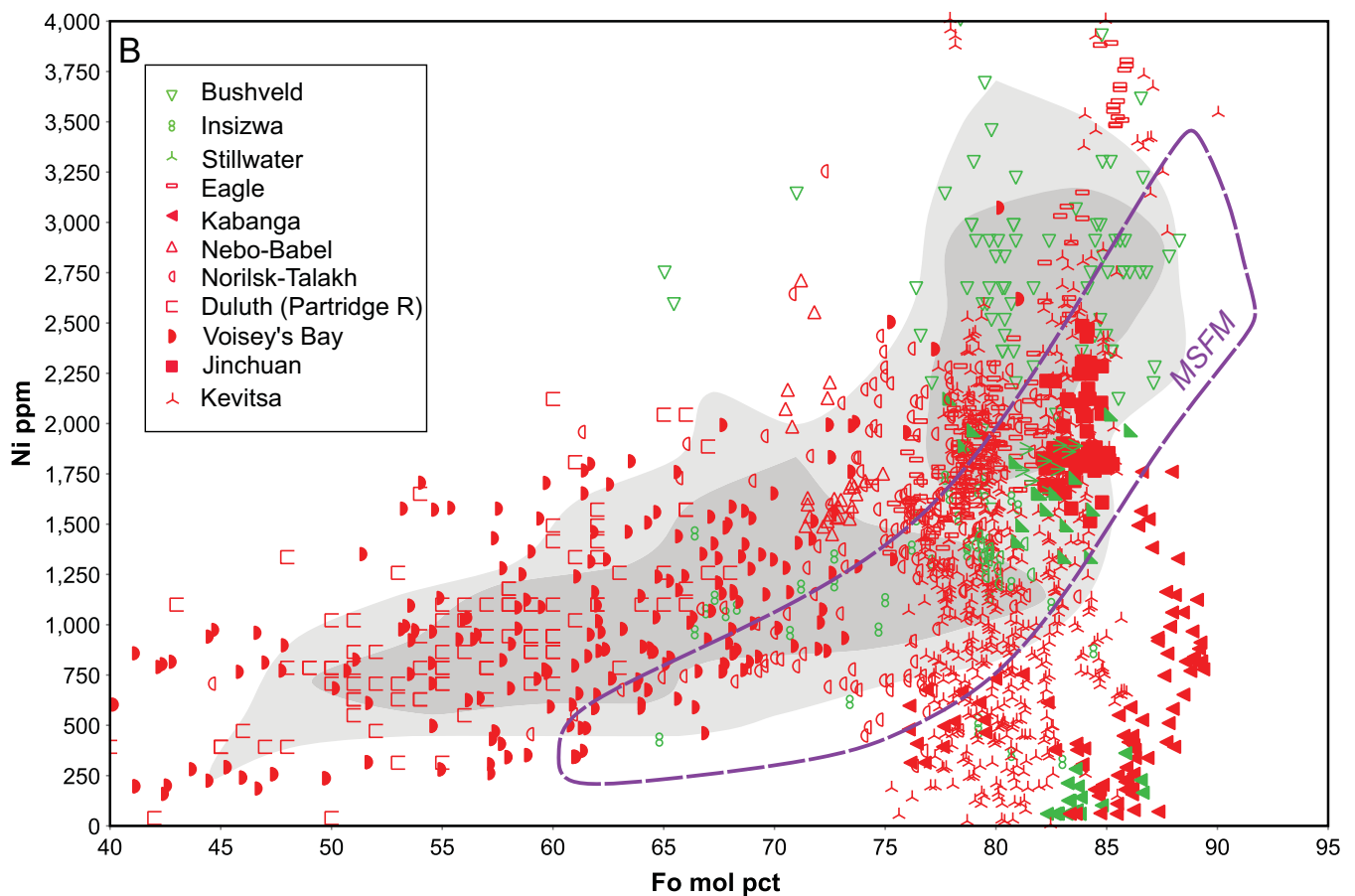
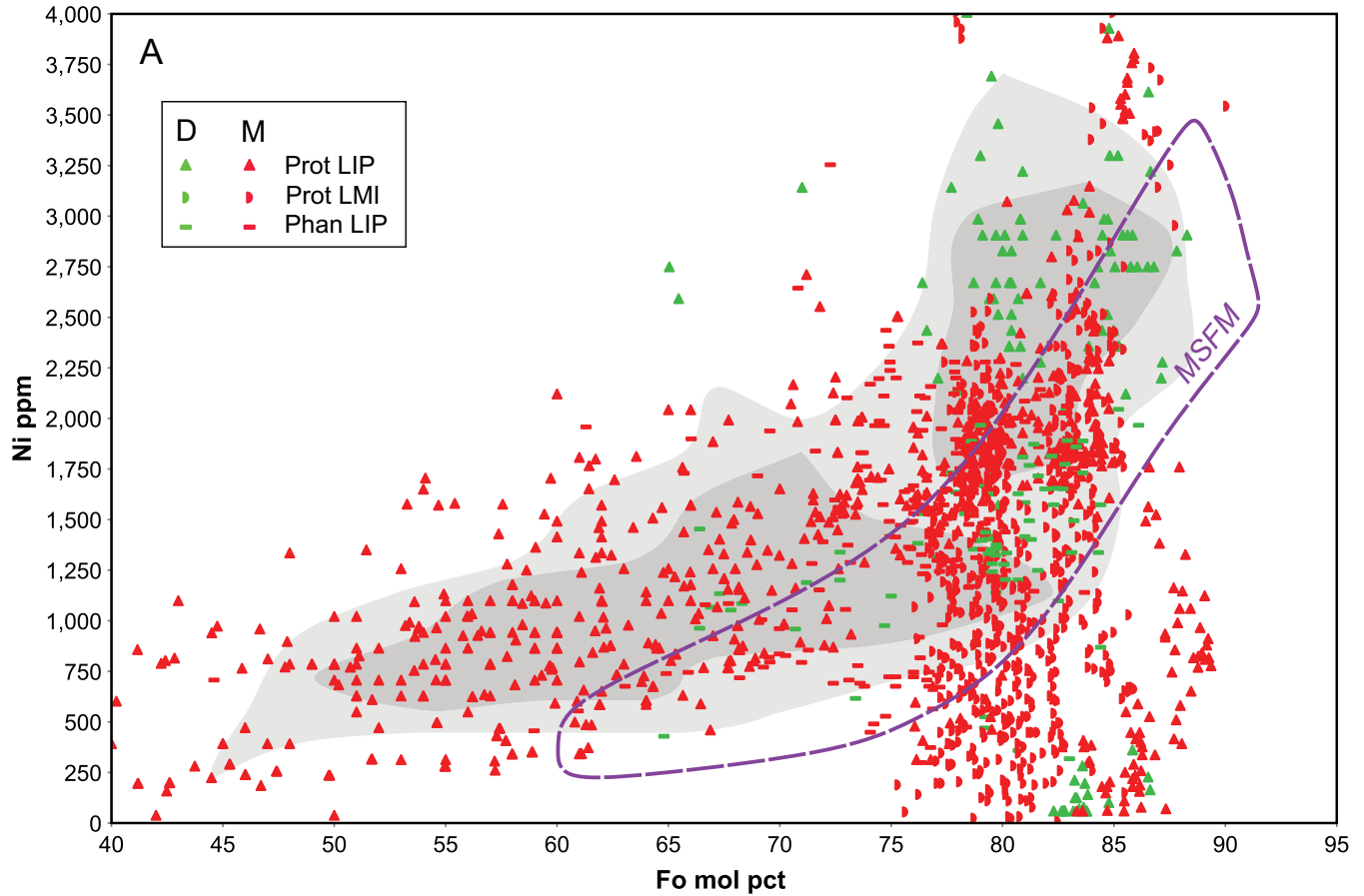


fig 4

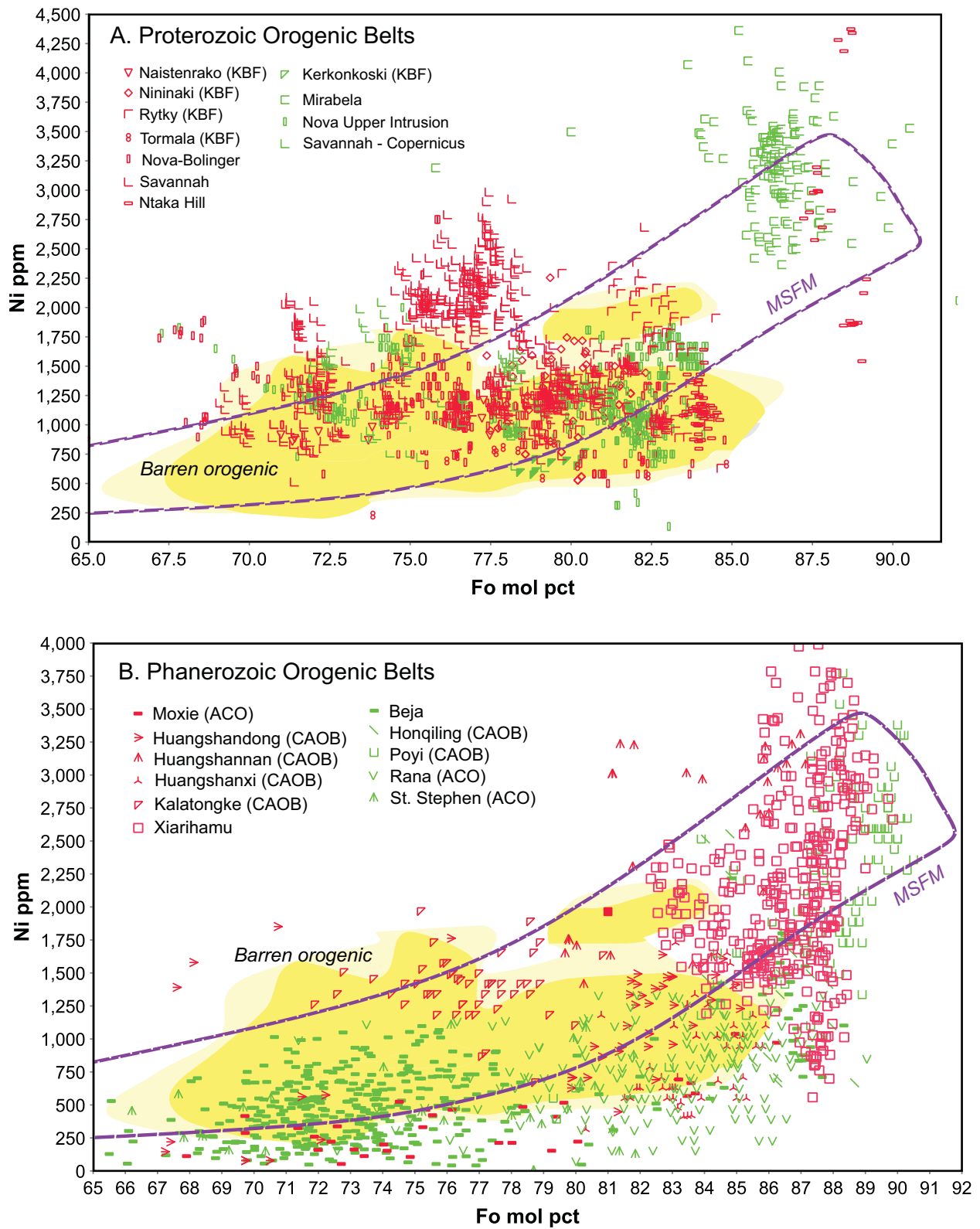


fig 5

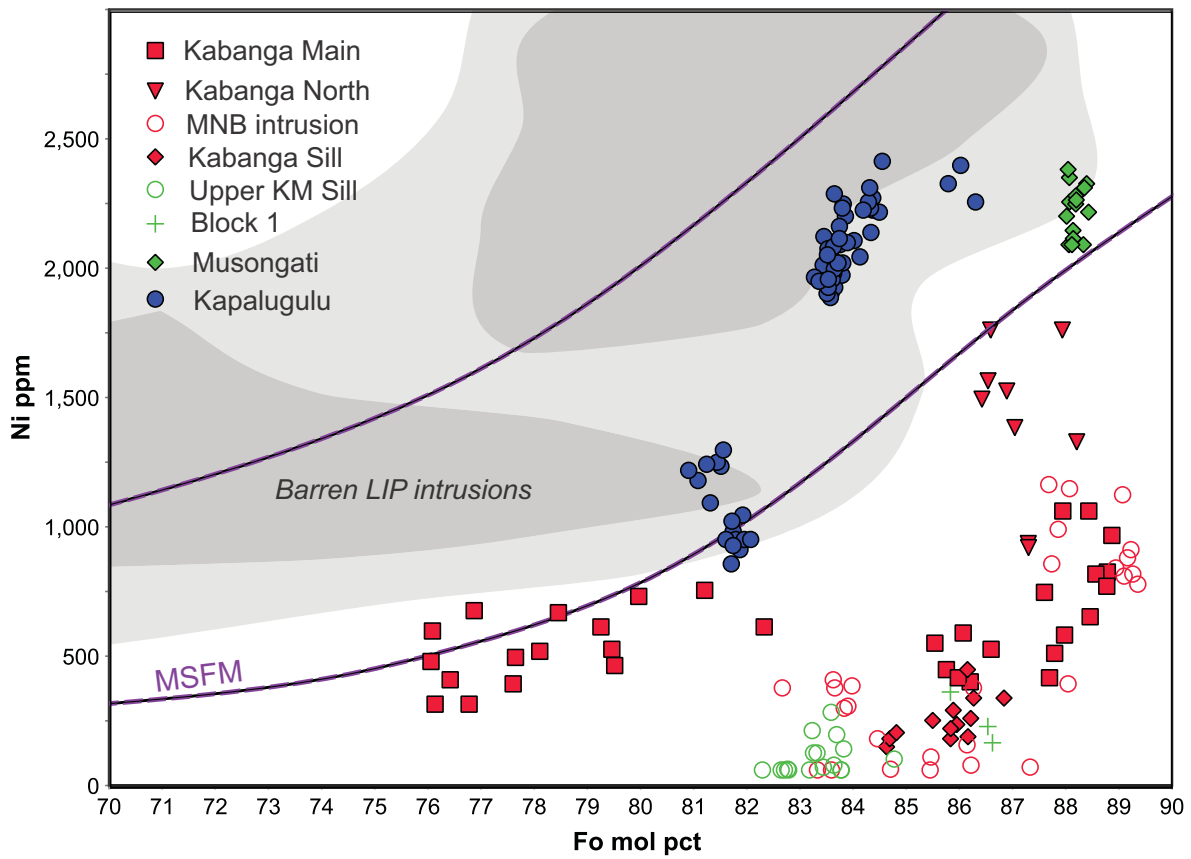


fig 6

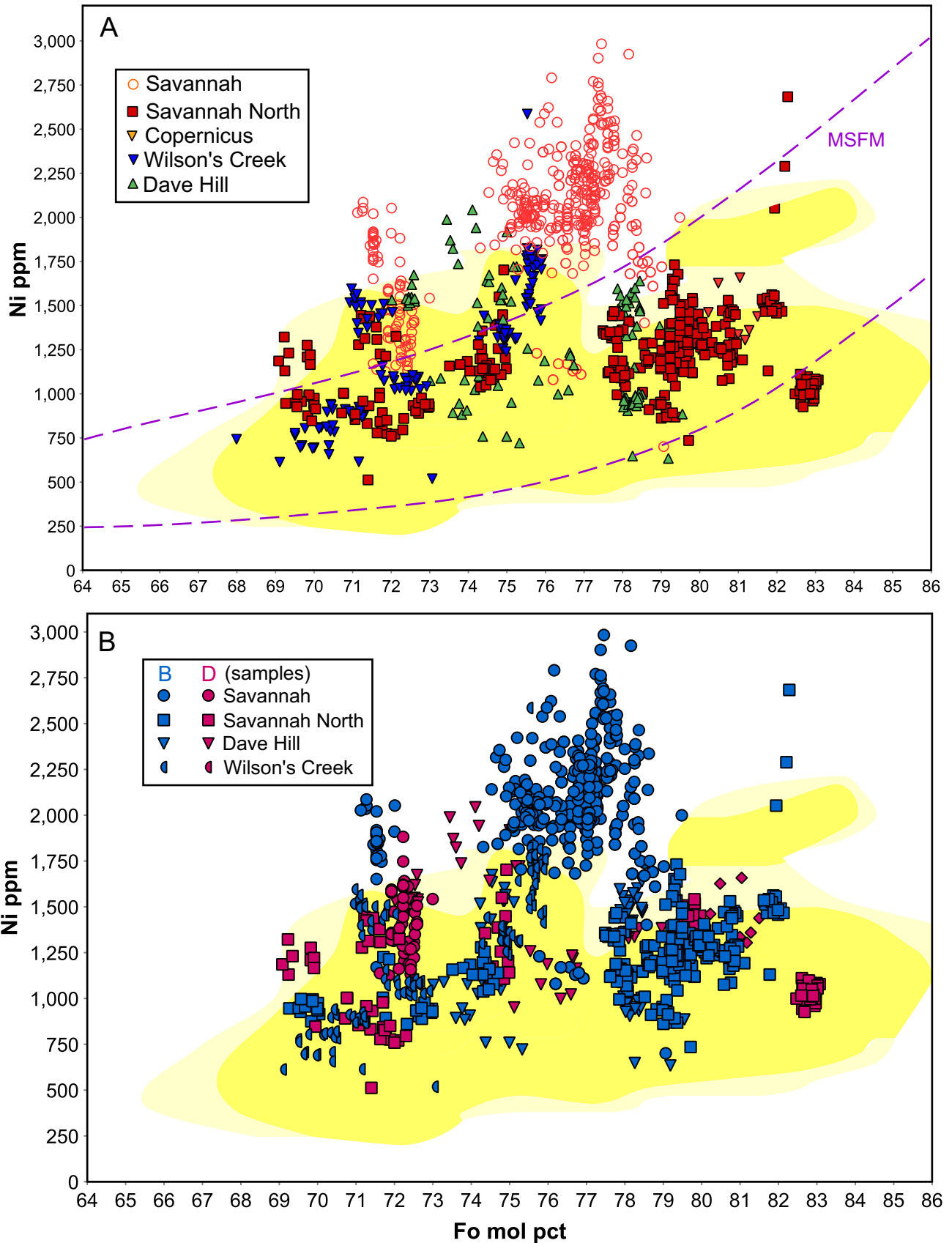


fig 7

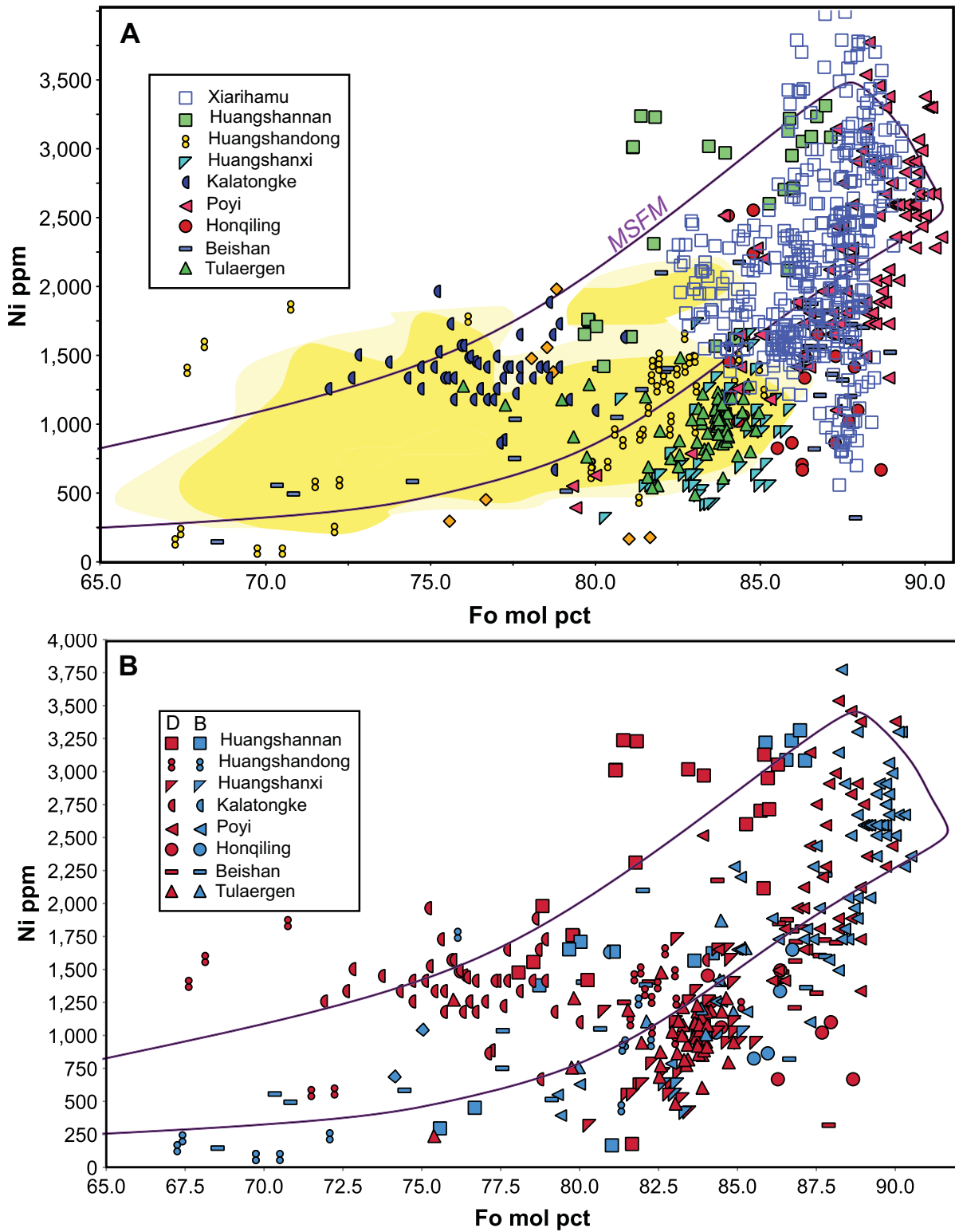


fig 8

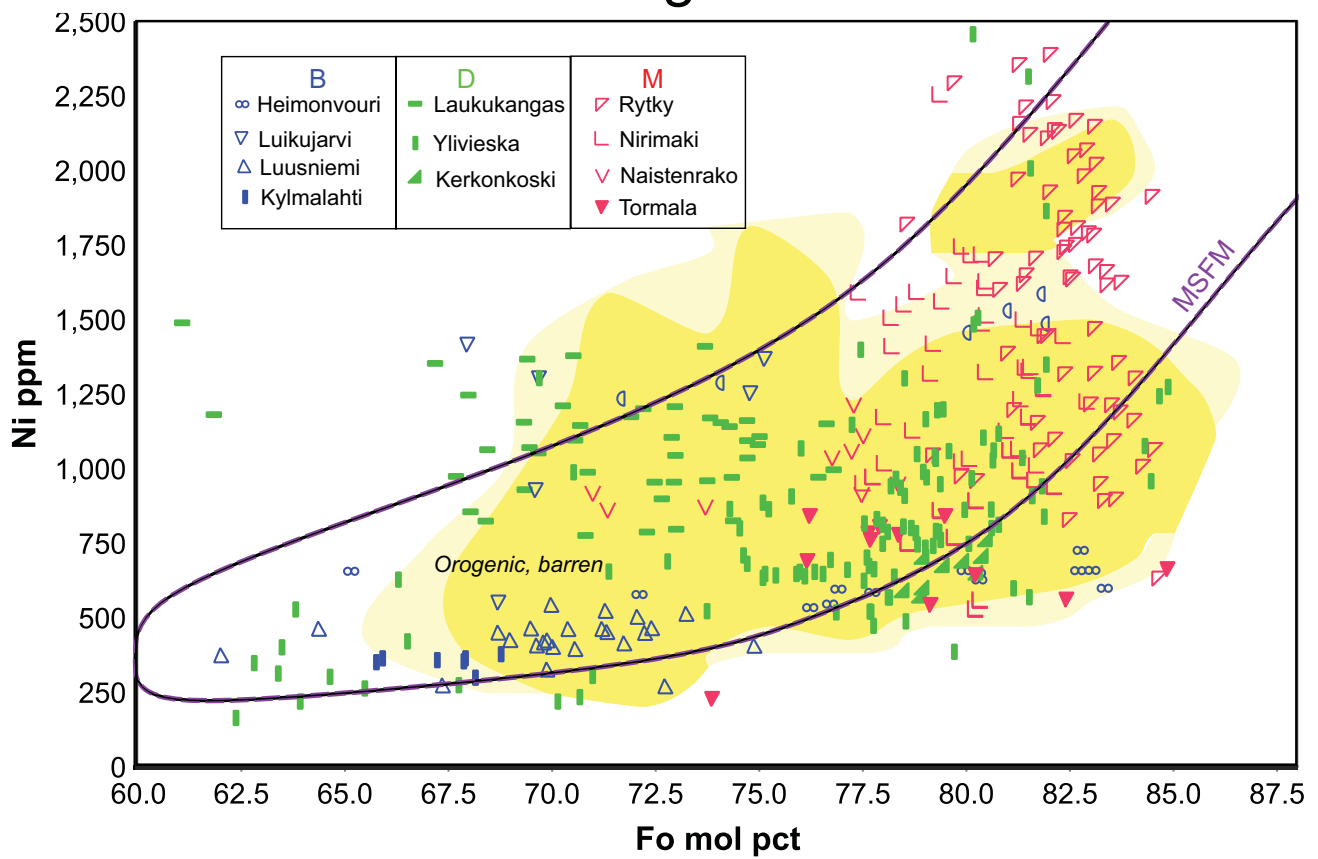


fig 9

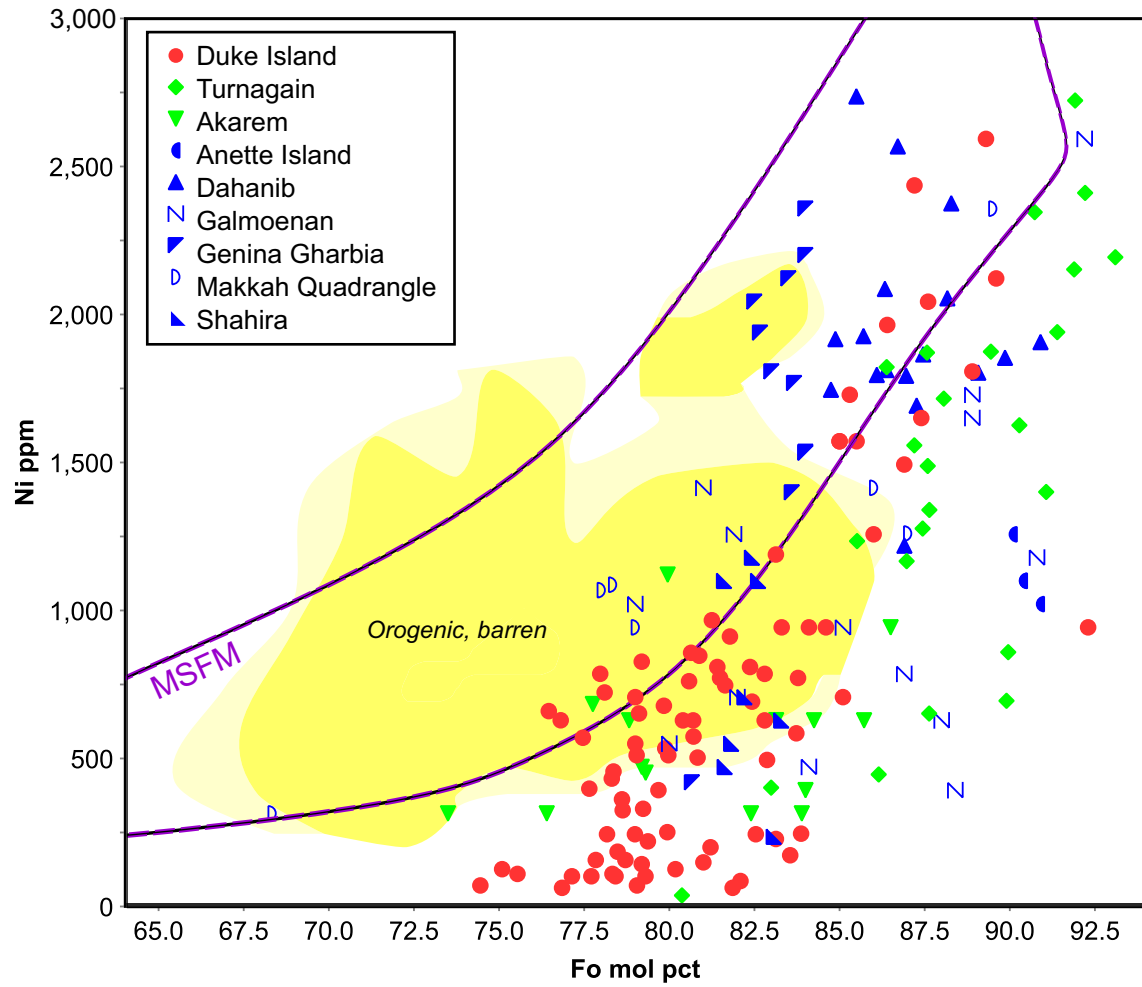


fig 10

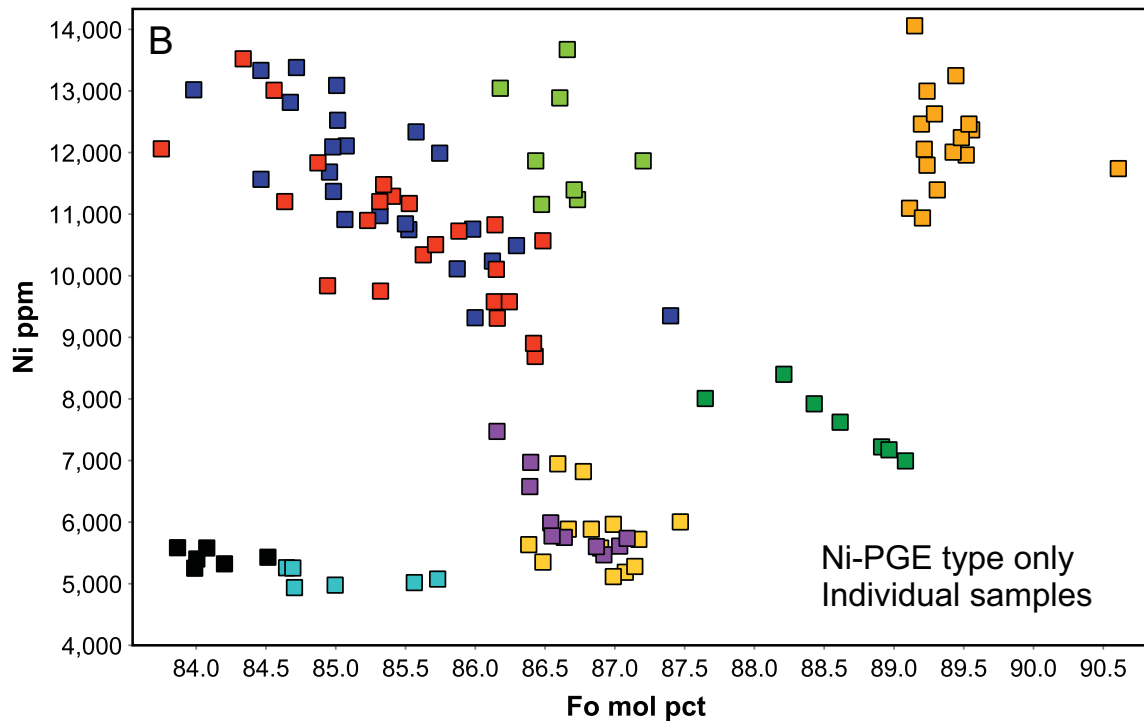
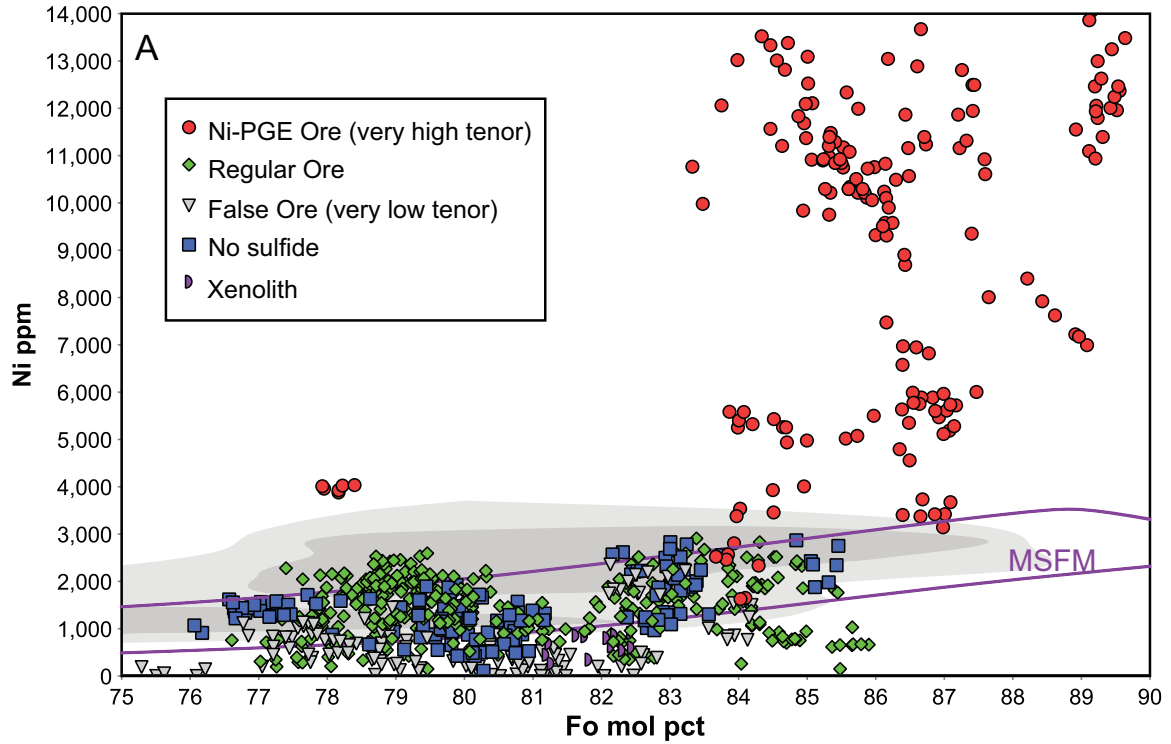
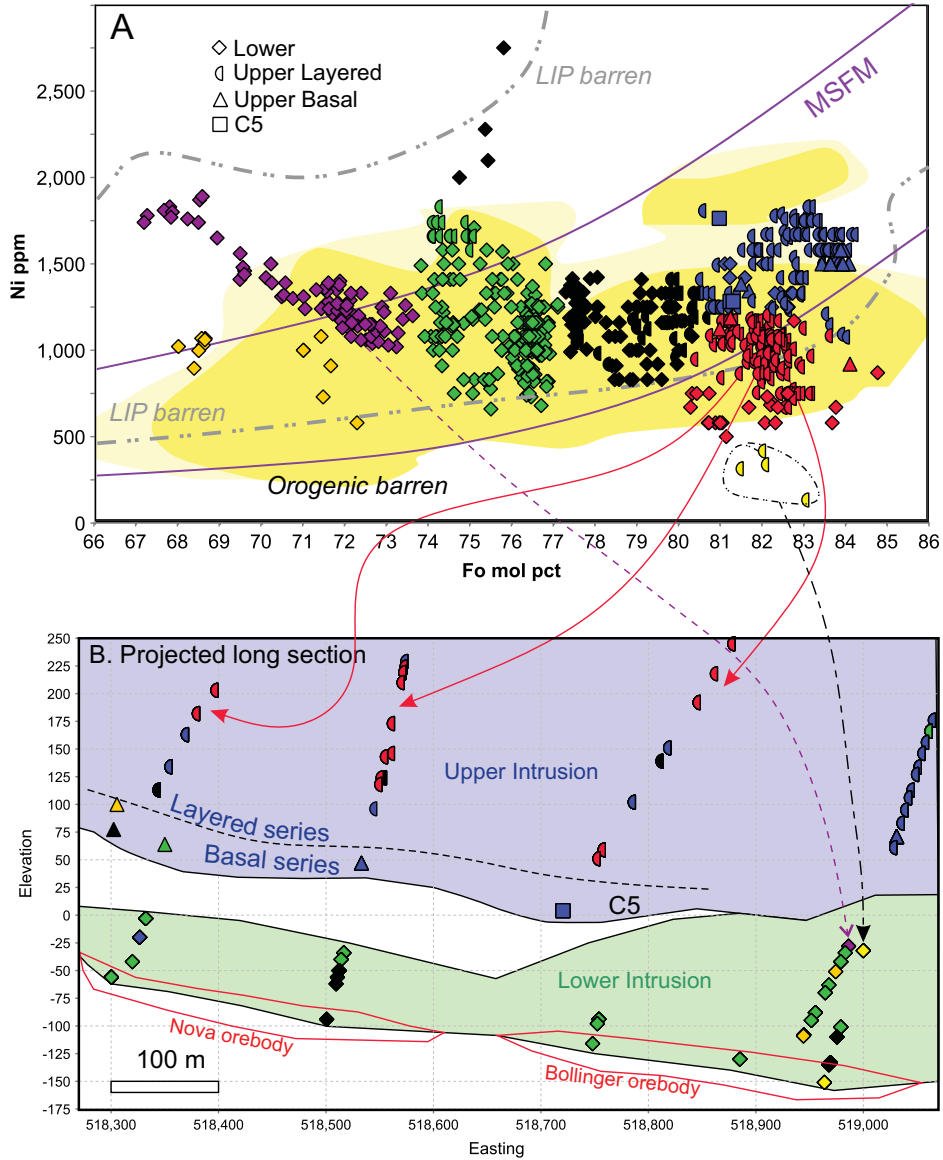


fig 11



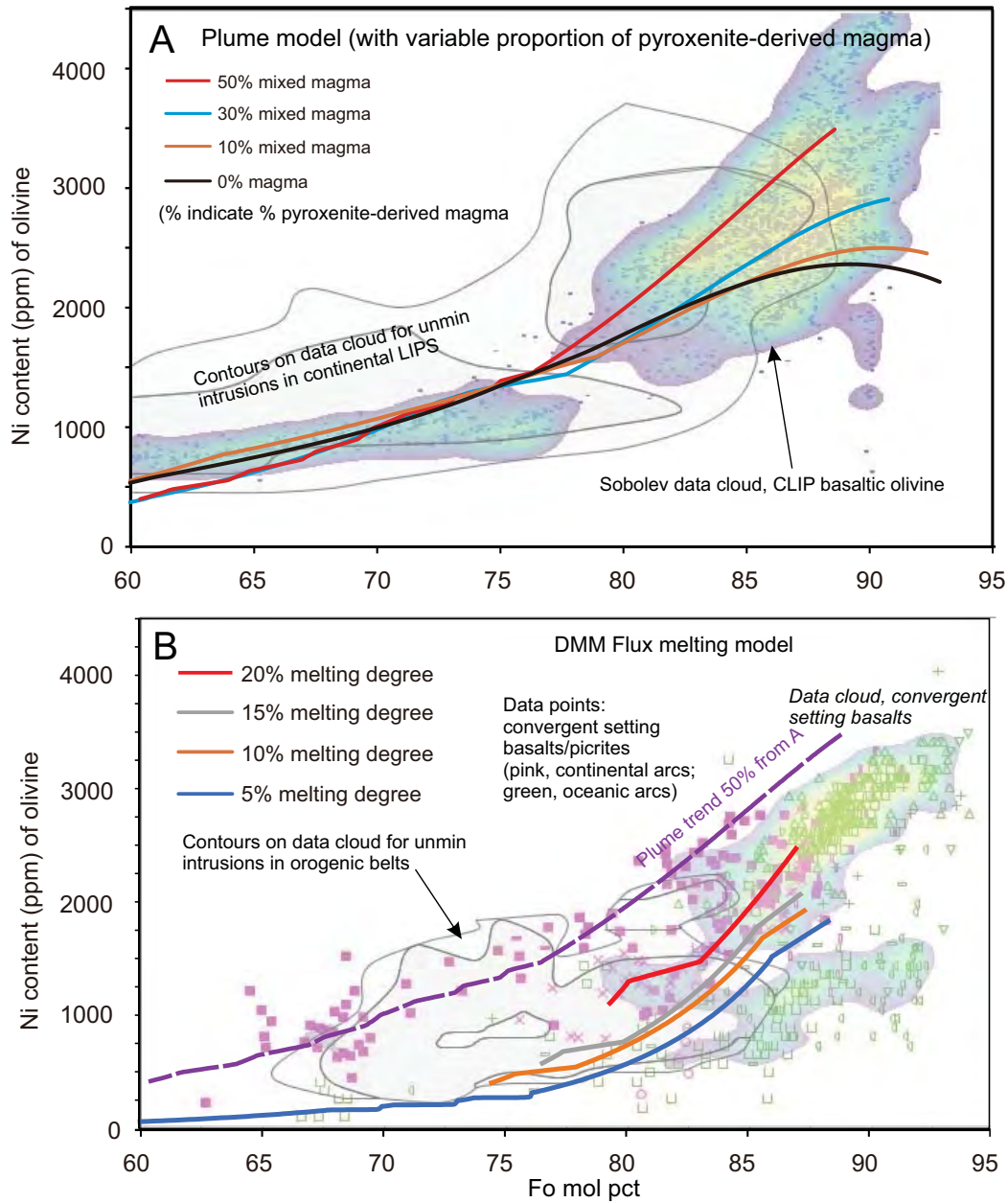


fig 13

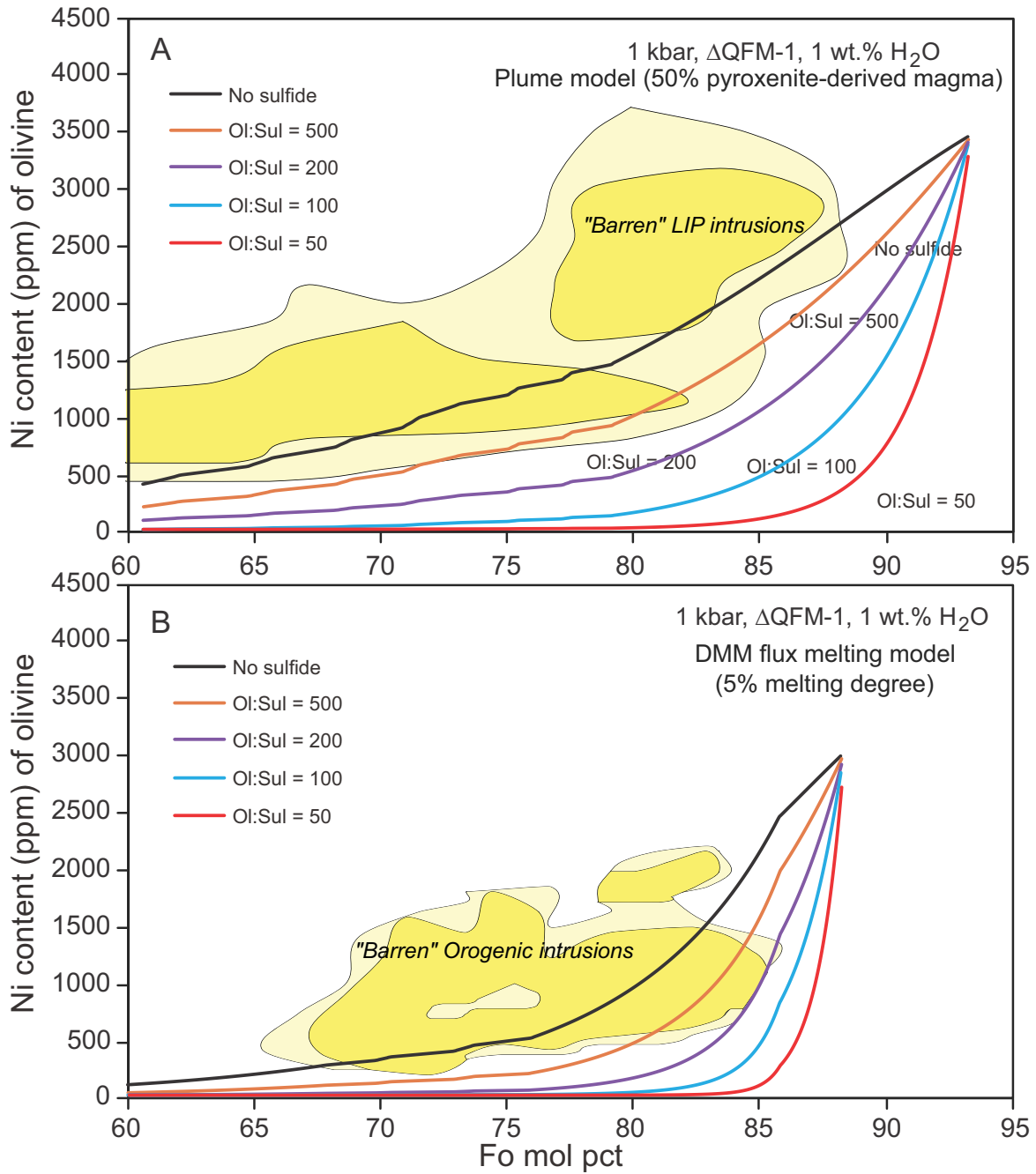


fig 14

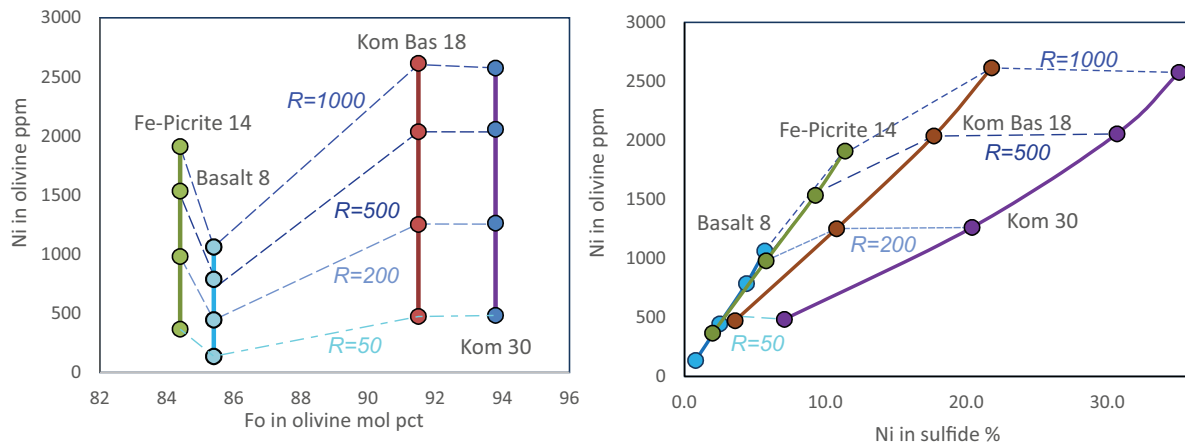


fig 15

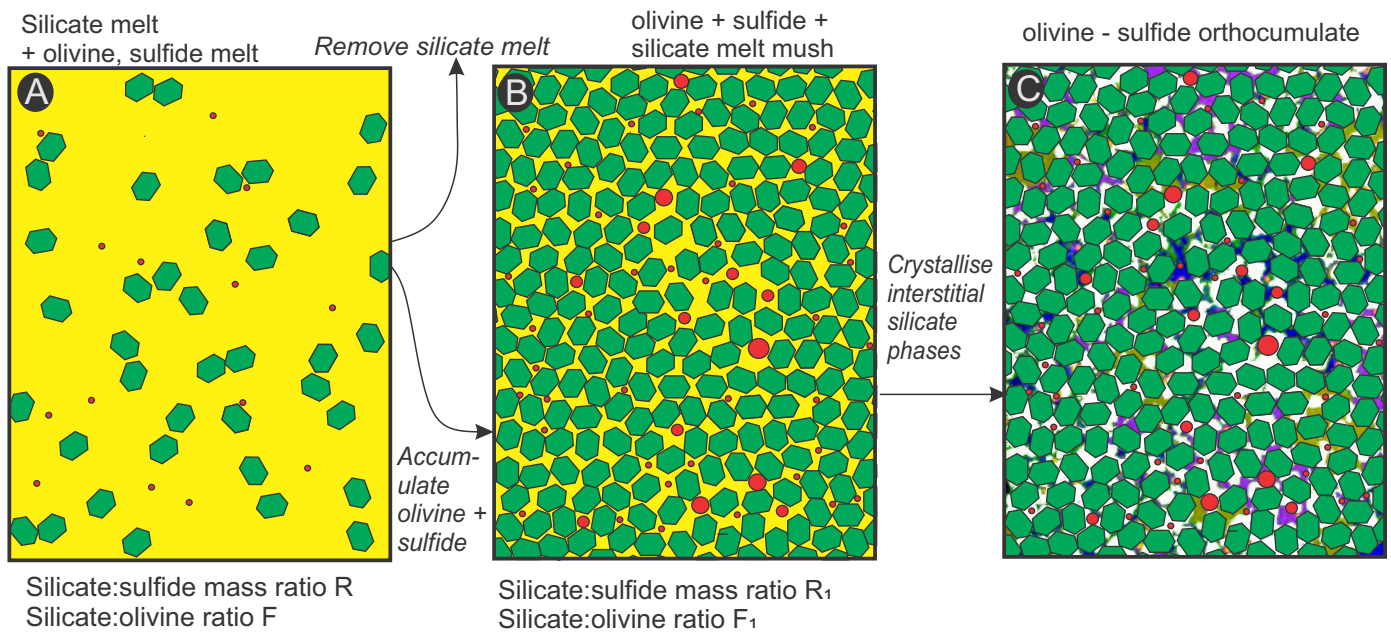


fig 16

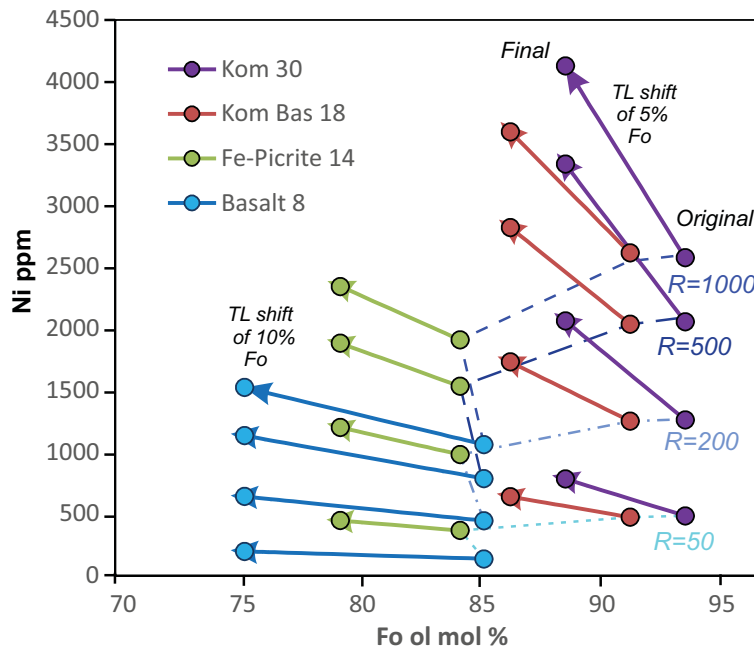


fig 17

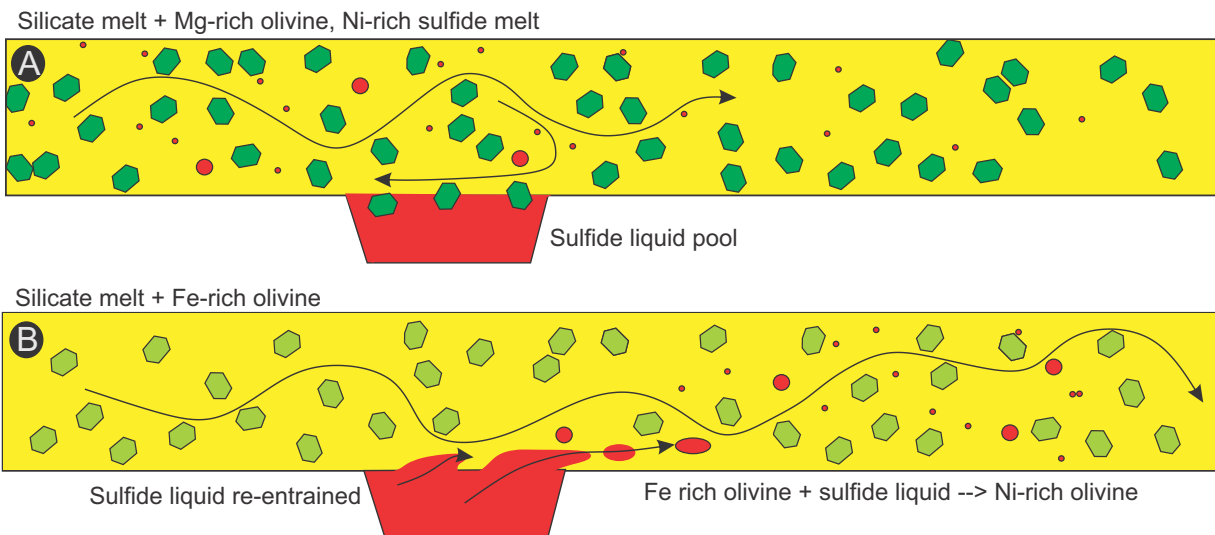


fig 18

